Scale invariant relationship between rainfall kinetic energy and intensity in Paris region: An evaluation using universal multifractal framework

Jerry Jose, Auguste Gires, Ioulia Tchiguirinskaia, Yelva Roustan, Daniel Schertzer

Scale invariant relationship between rainfall kinetic energy and intensity in Paris region: An evaluation using universal multifractal framework

Jerry Jose[a], Auguste Gires[a], Ioulia Tchiguirinskaia[a], Yelva Roustan[b], Daniel Schertzer[a]

[a]*HM&Co, École des Ponts ParisTech, 77455 Champs-sur-Marne, France*
[b]*CEREA, École des Ponts, EDF R&D, Île-de-France, France*

Abstract

To calculate the effect of rainfall in detaching particles and initiating soil erosion, or in eroding wind turbine leading edge, it is important to measure recorded drop size distributions (DSD) and fall velocity over long period. Commonly used relationships between kinetic energy (KE) and rainfall rate (R) exhibit strong dependence on the temporal resolution at which the analysis is carried out. Here we aim at developing a new scale invariant relationship relying on the framework of Universal Multifractals (UM), which is widely used to analyze and characterize geophysical fields that exhibit extreme variability across wide range of scales.

Rainfall data is collected using three optical disdrometers working on different underlying technologies (one Campbell Scientific PWS100 and two OTT Parsivel^2 instruments) and operated by the Hydrology Meteorology and Complexity laboratory of École des Ponts ParisTech in Paris area (France). They provide access to the size and velocity of drops falling through sampling areas of few tens of cm^2. Such data enables estimation of rainfall DSD, R and KE at various resolutions. The temporal variations of this geophysical data over wide range of scales are then characterized in the UM framework, which was never done for KE. A new power law relation is developed and tested against the theoretical

framework assuming gamma DSD for describing the dependence between KE and R. The developed equation using scale invariant features of UM does not rely on gamma DSD assumption, performs as well as the existing tools, and is valid not only at a single scale, but also across scales.

Keywords:

rainfall intensity, rainfall kinetic energy, disdrometer, multifractal, scale invariance, gamma DSD

---

1. Introduction

1.1. On the importance of rainfall and kinetic energy

Understanding the relation between rainfall rate (R) and kinetic energy (KE) is essential for accurate determination of various rainfall parameters and understanding their after effects on surrounding ecosystem (Karlen et al., 2003). It has been well established that onsite erosion of soil - splash and runoff - depends on drop size distribution (DSD) and fall velocity of the spectrum (Ellison, 1944; Fernández-Raga et al., 2017). Hence, KE and R are primarily used to quantify rainfall erosivity and to estimate erosion rates in universal models towards sustainable land use planning (Angulo-Martínez et al., 2012; Shojaei et al., 2020; Mohamadi and Kavian, 2015). Erosion heavily affects agricultural sector: On on-site level, it impoverishes the top soil off nutrients and organic matter along with their water holding capacity; this in turn increases the use of fertilizers and hence causes pollution at the recipient end of off-site erosion. Further, on off-site level, soil transport by erosion can trigger flood events through silting up of basins and rivers (Pimentel, 2006; Enne et al., 2000). Rainfall erosivity is a key parameter in various erosion models such as US based Universal Soil Loss Equation (USLE, Smith and Wischmeier, 1962) and its revised version (RUSLE, Renard et al., 1997), South Korean based SEMMA models for calculating soil loss (Deog Park et al., 2012), and in European models such as EUROSEM, WaTEM etc. that account for sediment transportation along soil loss (Morgan et al., 1998; Van Oost et al., 2000; Kirkby et al., 2008, an advance on USLE). Most of these frameworks use KE as the major quantifying factor for estimating erosivity at spatial scales as rainfall KE represents the total energy available for detachment and transport of soil on surface of impact. As direct measurement of KE is limited to specific geographical locations possessing required instrumental capabilities, understanding the relationship between KE and the more

commonly available rainfall parameter, R, is important in estimating the former in more places.

Accurate estimation of rainfall KE is also important in understanding and mitigating leading-edge erosion (LEE) on wind turbine blades. Erosion damage reduces aerodynamic performance of blades resulting in reduced annual energy production and increased down-time (Keegan et al., 2013). Though LEE involves a multitude of atmospheric factors, impact velocity and amount of precipitation have been established as some of the major external factors in erosion (Herring et al., 2019). As in soil erosion, larger drops with greater mass and vertical terminal velocity causes a disproportionate amount of erosion in LEE also. Rainfall KE helps to quantify the impact of droplets hitting perpendicular to the surface and hence rainfall erosion on blades which is the accumulated aggregate of multiple impacts stochastically distributed over the surface of the coated laminate (Bech et al., 2018). In Whirling arm rain erosion test (WA-RET) (ASTM-G73-10, 2017; Liersch and Michael, 2014; DNVGL-RP-0171, 2014), the industrial standard for measuring durability of leading-edge structures, specimens are subjected in controlled velocity and rain conditions to assess the damage caused by droplet impacts (Bech et al., 2018). Considering the rapid growth of offshore wind industry as sustainable clean energy solution in the Americas and Asia with monsoon seasons, proper representation of KE and R is important in quantifying LEE in wind turbines.

1.2. Review of existing relations and need for a scale invariant representation

Application of erosion frameworks such as USLE or RUSLE poses uncertainties because of their empirical basis which has single or limited measurement locations and specific methods of data collection. These frameworks take KE as the major quantifying factor for erosivity, and employ various corrections to mitigate overestimation at low inten-

sity rainfall as smaller droplets are less effective in soil detachment (van Dijk et al., 2002). Another commonly used erosivity index is rainfall momentum, but it has been shown that for natural rainfall they exhibit similar relationship with rainfall intensity (Hudson, 1971). These models are based on traditional two parameter exponential rain drop size distribution models developed from smaller sample collection methods such as flour pellets or stain paper (Laws and Parsons, 1943; Marshall and Palmer, 1948). Later studies using multi parameter radiometry and disdrometers have shown improvements in measurement if DSD is assumed to be a three parameter gamma distribution (Ulbrich, 1983). Gamma distribution assumes fewer large drops in rain and represents a narrower DSD than the exponential one, and thereby reduces the overestimation of KE by the latter. For recording DSD and in turn obtaining empirical KE, disdrometers are commonly used in meteorological campaigns, where fall velocity is either directly measured or estimated from empirical relations (Gunn and Kinzer, 1949; Atlas et al., 1973).

There has been various studies towards accurate representation of $KE - R$ relationship. Fox (2004) demonstrates the impact of formulation of DSD in calculation of KE and hence on erosion. Smith and Wischmeier (1962) proposed a logarithmic function based on DSD formulation by Laws and Parsons (1943) and terminal velocity by Gunn and Kinzer (1949). It was used in modelling erosion in USLE, which was later replaced by continuous exponential functions in revised USLE approach (Renard et al., 1997; Brown and Foster, 1987). Other proposed forms of $KE - R$ equations were linear (Kinnell, 1981; Sempere-Torres et al., 1998), polynomial (Carter, 1979) and power-law (Park et al., 1982). Critical literature appraisal by van Dijk et al. (2002) on various $KE - R$ relations lists measurement techniques and procedures, sampling biases, interpretation methods and storm types as reasons for discrepancies and suggests another exponential based predictive equation. More recent

reviews such as Angulo-Martínez and Barros (2015), Wilken et al. (2018), Mineo et al. (2019) shows lack of universality among various $KE-R$ relationships (logarithmic, linear, power law and exponential) using disdrometer measurements and modelling at different geographic stations, meteorologic conditions and time aggregation used for calibration.

Most of the empirical formulations express KE as volume specific - kinetic energy per unit area and mm of rainfall or KE_{mm} ($\mathrm{J\,m^{-2}\,mm^{-1}}$) due to prevalence of non automated measurements and lack of accuracy in determining exposure time. But expression of volume specific kinetic energy creates a statistical artefact (spurious ratio correlation) in $KE-R$ relationship due to the inclusion of R ($\mathrm{mm\,h^{-1}}$) in the KE_{mm} expression. Salles et al. (2002) suggests usage of more consistent time specific KE or KE_{time} ($\mathrm{J\,m^{-2}\,h^{-1}}$) that has been shown to produce less heteroscedasticity than corresponding $KE_{mm}-R$ scatter plots. For representing erosion, KE_{time} has been expressed as the rate of expenditure of rainfall kinetic energy (Kinnell, 1981), rainfall or kinetic power (Smith and De Veaux, 1992) and rainfall kinetic energy flux density (Steiner and Smith, 2000). The two expressions are related to each other through rain intensity and hydrological studies usually harmonize $KE-R$ relationships with KE_{time}.

$$KE_{time} = R \times KE_{mm} \tag{1}$$

In this paper the expressions for KE are derived and analyzed in the form of KE_{time} unless otherwise specified.

Due to variations in methodologies used and DSD characteristics during measurement, different functional forms show different behaviour towards $KE-R$ estimation. Though commonly preferred, exponential relations have been shown to underestimate KE_{time} for lower intensities of rainfall (Carollo and Ferro, 2015). Power-laws that predict kinetic

energy well at lower intensities tend to overestimate the same for higher intensities. Logarithmic curves are limited in their usage though they fit low and high intensity KE rather decently (van Dijk et al., 2002). Further due to the empirical formulation, when it comes to expressing KE_{time} vs R, most of these mathematical equations fail to have much physical justification. Using generalized scaling formulation that expresses various existing DSD models as it's special cases (Torres et al., 1994; Sempere-Torres et al., 1998), Salles et al. (2002) found that power law is the most suitable function to relate KE_{time} and R from a microphysical point of view. The parameters (prefactor and exponent) of power law are related to rain type, geographical location and measuring technique. Shin et al. (2016) has proposed a representative power law based on the ideal assumption that the drop-size is uniformly distributed under the constant rainfall intensity.

1.3. Purpose of paper

Current literature on KE and R lacks a common consensus on the usage of expression that is valid across various scales of measurement, hydro-meteorological regimes or observation techniques. There is an increased focus on research characterizing rainfall microphysics at local and regional scales (Petan et al., 2010). Here we examine the variation of KE and R for over 7 years in Paris region using continuous data from three disdrometers from two different manufacturers. Using the framework of Universal Multifractal (UM) (Schertzer and Lovejoy, 1987), efforts were made to characterize the variability of KE_{time} and R on event based and year based analysis, and to formulate a scale invariant relation based on power law relationships. Multifractals allow characterization of complex geophysical fields with a limited number of scale invariant exponents (see Schertzer and Tchiguirinskaia, 2020, for a recent review). Multifractal behaviour of measured rainfall has been abundantly studied previously (see Gupta and Waymire, 1990; Kumar and

Foufoula-Georgiou, 1993; Deidda et al., 1999; Olsson and Niemczynowicz, 1996; García-Marín et al., 2008; Langousis et al., 2009; Emmanouil et al., 2020, for some examples among others). Wolfensberger et al. (2017) & Schertzer and Lovejoy (2011) used UM in climatological analysis of precipitation - modelled and actual - in relation to external geographical and meteorological descriptors. Checking the validity of UM framework on KE, which was never done to the knowledge of the authors, is a first goal of the paper. The main goal of this paper is to explore the possibility of establishing a physically based scale invariant power law relationship between KE and R using the UM framework, without having to rely on strong assumptions on DSD shape; and compare its performance with more classical approach.

This article is structured as follows. In section 2 the methodology used is detailed. First, the commonly used framework of gamma distributed DSD which yields a power-law relation is reminded along with the associated parameters' estimation techniques. Then, the process to identify power-law relation in the UM framework is explained after a required reminder on the theoretical underlying basis. Similarly, the associated parameters' estimation techniques, which will be implemented, are described. Section 3 includes details of data collection and quality control. Results are discussed in section 4 where validity of formulated relation is tested and contrasted over different types of rain events. The final section, section 5, concludes the study and summarizes the main observations.

2. Methodology

2.1. Theoretical relation assuming gamma distributed DSD

2.1.1. Rainfall microstructure and commonly used gamma distribution

Rainfall is measured and represented as distribution of raindrops in different diameter classes or drop size distribution (DSD) and their corresponding terminal fall velocity in stable air. For meteorological purposes, size distribution of raindrops is represented as mean number of drops per unit volume in a particular diameter (more precisely equivolumic diameter, i.e. the diameter of a drop with the same volume but a spherical shape) range between D and $D+dD$, $N_v(D)$ (m^{-3} mm^{-1}). However, in hydrological studies, DSD measured by ground based devices such as disdrometers or optical spectrometers are represented as mean number of raindrops in a particular diameter range arriving at a surface per unit area per unit time, $N_A(D)$ (m^{-2} mm^{-1} s^{-1}). If effects of wind, turbulence and raindrop interactions are neglected, $N_v(D)$ and $N_A(D)$ are related as follows (Uijlenhoet and Stricker, 1999) :

$$N_A(D) = v(D)N_v(D) \tag{2}$$

where $v(D)$ represents the terminal fall velocity ($\mathrm{m\,s}^{-1}$) as a function of the equivalent spherical diameter of raindrop D (mm).

Traditional mathematical expressions describing $N_v(D)$ such as exponential (Marshall and Palmer, 1948), weibull (Best, 1950), gamma (Ulbrich, 1983) and lognormal (Feingold and Levin, 1986) can be expressed as particular case of general formulation proposed by Sempere-Torres et al. (1998). For the scope of this paper, gamma distribution of DSD, which has been recognized to better represent natural rain, will be considered (Ulbrich,

1983). In this framework :

$$N_v(D) = N_0 D^{\mu} e^{-(\Lambda D)} \tag{3}$$

where $N_v(D)$ is in $\mathrm{m}^{-3}\,\mathrm{mm}^{-1}$, D in mm, N_0 (in $\mathrm{m}^{-3}\,\mathrm{mm}^{-1-\mu}$), μ and Λ (in mm^{-1}) are distribution parameters measuring raindrop concentration, mean size and shape of spectrum respectively. Λ is usually expressed with the help of the median volume diameter D_0 as $\Lambda = (3.67 + \mu)/D_0$.

2.1.2. Theoretical power law relation between R and KE

Rainfall intensity or rain rate (R, in $\mathrm{mm\,h}^{-1}$) can be calculated from $N_A(D)$ using following expression (Steiner and Smith, 2000) :

$$R = 3.6 \times 10^{-3} \frac{\pi}{6} \int_0^{\infty} D^3 N_A(D) dD \tag{4}$$

Kinetic energy per unit area per unit time (KE_{time} in $\mathrm{J\,m}^{-2}\,\mathrm{h}^{-1}$) of falling drops can also be expressed in terms of measured $N_A(D)$ as follows (Steiner and Smith, 2000) :

$$KE = 3.6 \times 10^{-6} \frac{\pi \rho}{12} \int_0^{\infty} D^3 v^2(D) N_A(D) dD \tag{5}$$

where ρ is density of water in standard conditions in ($\mathrm{kg\,m}^{-3}$).

Though there are more sophisticated equations proposed in the literature for $v(D)$, for simplicity in calculation, here we are following the widely used power law formulation by Atlas and Ulbrich (1977). Uijlenhoet (2001) demonstrated it has the only functional form consistent with power law relationship between rainfall related parameters :

$$v(D) = c\,D^{g} \tag{6}$$

$c = 3.78\,\mathrm{m\,s^{-1}mm^{-g}}$ and $g = 0.67$ (with v in $\mathrm{ms^{-1}}$ and D in mm).

Most of the rainfall parameters can be approximated as moments of the DSD; and when DSD follows gamma model, the n^{th} moment, M_n can be computed as (Atlas and Ulbrich, 1977) :

$$M_n = \int_0^{\infty} D^n N(D) d(D) = N_0 \Lambda^{-(\mu+n+1)} \Gamma(\mu+n+1) \tag{7}$$

where $\Gamma(\alpha)$ is the complete gamma function

$$\Gamma(\alpha) = \int_0^{\infty} x^{\alpha-1} e^{-x} dx, \quad \text{where } \alpha > 0. \tag{8}$$

Substituting equations 2, 3, 6 and 7, and solving the integral gives reduced expressions for KE and R in terms of gamma function;

$$R = 6 \times 10^{-4} \pi c N_0 \frac{\Gamma(4+g+\mu)}{\Lambda^{(4+g+\mu)}} \tag{9}$$

$$KE = 3.6 \times 10^{-6} \frac{\rho \pi c^3}{12} N_0 \frac{\Gamma(4+3g+\mu)}{\Lambda^{(4+3g+\mu)}} \tag{10}$$

This reduction using gamma function enables representation of KE and R in the form of a power law as follows :

$$KE = bR^{a} \tag{11}$$

where

$$a = \frac{4+3g+\mu}{4+g+\mu}$$
$$b = 5\times10^{-4}\rho c^2\left[6\pi cN_0\times10^{-4}\right]^{1-a}\frac{\Gamma(4+3g+\mu)}{(\Gamma(4+g+\mu))^a} \tag{12}$$

The final expression follows the same pattern as that by Salles et al. (2002) based on generalized DSD and that of Uijlenhoet and Stricker (1999) based on exponential DSD. When $\mu = 0$ gamma distribution for DSD becomes a simple Marshall and Palmer negative exponential parameterization representation of DSD (Marshall and Palmer, 1948) with Eq. 11 becoming $KE = 8.539R^{1.287}$. Same values were obtained for exponent 'a' and pre-factor 'b' using the general function proposed by Salles et al. (2002) for Marshall and Palmer approximation. Closer value of exponential coefficient were also reported by Uijlenhoet and Stricker (1999) in a power law formulation based on Marshall and Palmer (1948) approximation of DSD and power law dependence of rain drop terminal velocity, Eq. 6 (Atlas and Ulbrich, 1977).

Many simplifications were followed in this formulation of KE-R relation as a power law (Eq. 11). Gamma DSD is notably assumed as well as a power law form for terminal fall velocity as function of diameter. This approximation shows limitations at higher values of diameter ($D > 5$ mm) and doesn't account for atmospheric turbulence or updrafts and downdrafts (Adirosi et al., 2016). Effect of truncation errors in measurement is not considered. The formulation also ignores the effect of horizontal wind velocity and surface impact angle of rain drops. Some authors tend to consider normalized spectra of DSD (Testud, 2001) that requires only two parameters to describe the DSD; it was also not considered here for the sake of simplicity in deriving a theoretical relation between KE and R. It should be noted that although widely accepted as the best representation of natural DSD,

gamma function also has associated errors that exists outside experimental methodology and sampling (Adirosi et al., 2014).

2.1.3. Estimation of power law coefficients from gamma DSD parameters

As mentioned before, most rainfall parameters can be expressed as moments of the DSD according to Eq. 7. The right hand side of the equation is specific to the non normalized three parameter gamma distribution considered here, as shown in Eq. 3. In practice DSD is not measured continuously but for discrete diameters D_i. As a consequence, the estimated moments $\hat{M}_n$ of order n are computed thanks to the following discrete sum rather than previous integral :

$$\hat{M}_n = \sum_{i=1}^{N_{class}} D_i^n N_i(D_i) \Delta D_i \qquad [\mathrm{mm}^n \mathrm{m}^{-3}] \tag{13}$$

where D_i is the diameter of droplet in class i, $N_i(D_i)$ is the drop size distribution (estimation discussed later in Eq. 26), ΔD_i is the width of diameter class i and N_{class} the total number of diameter classes.

Investigation of various DSD parameter estimating methods by Cao and Zhang (2009) highlighted the risk in usage of maximum likelihood and L-moment estimators for processing data with truncation in lower end of DSD spectra. As all disdrometers are limited by some minimum value of measurable diameter D_{min} (> 0), it is advisable to use traditional method of moments (Brawn and Upton, 2008). Although the choice of moments for proper parameters estimation with the method of moments is a relevant topic, it is outside the scope of this paper. Hence, authors relied on the existing literature. More precisely, although higher DSD moments are considered to be associated with higher errors, the tendency of lower errors with middle order moments was shown later in Smith et al. (2009)

(using radar measurements) and Cao et al. (2008) (using joint disdrometer-radar observations). Cao and Zhang (2009) evaluated the performance of various moment estimators using simulations of gamma DSD (with a more realistic estimation of errors) and found that second, third and fourth moments (M234) as the best overall performer for estimating R. Konwar et al. (2014) (M234) and Huang et al. (2021) (even higher order moments - 2,3 and 6) are some recent examples of using middle order moments while analysing data from same disdrometer make as the one in current study (OTT Parsivel^2). Hence, it was chosen to employ these moments for computing gamma DSD parameters: μ, N_0 and Λ (refer Eq. 7). Specific moment equations are provided in the appendix (Appendix B). These parameters are then introduced in Eq. 12 to derive the expected power law parameters assuming a gamma DSD.

Variation of a and b with DSD parameters is examined with available data set in section 4 for different type of rainfall events.

2.2. Theoretical relation between multifractal fields in UM framework

2.2.1. Overview of the theoretical framework

The framework of Universal Multifractals (UM) enables to characterize the extreme variability of geophysical fields across scales, with the help of a limited number of parameters with physical meaning (Schertzer and Lovejoy, 1987). It relies on the assumption that these fields are generated through an underlying multiplicative cascade. Such behaviour is assumed to be inherited from the scale invariant features of the Navier-Stokes equations, but has not yet been formally showed. Consequently, statistical properties of fields are conserved in all scales. In this study, time specific kinetic energy and rainfall intensity from disdrometer measurements are analyzed using UM. Review by Schertzer and Lovejoy (2011) discusses the techniques and methodologies employed in more detail.

For analysis in UM framework, the field in consideration is normalized (divided by its mean value) and its total size in terms of numerical values is restricted to be a power of two. The field can be one or two dimensional; since current study involves only time series we will be limiting our discussion to single dimension. Let us consider a normalized conservative field (an additional parameter for non-conservative fields is introduced later) ε_λ at resolution λ. Resolution λ is the ratio of L, the outer scale, to l, the observational scale. Let us first consider the occurrence pattern of the field, i.e. the same field with 1 for strictly positive values and 0 otherwise. If the field is fractal, then the probability p that a segment of length l intersects the field (p is the probability of occurrence of non zero elements in the total binary field) scales with resolution as follows:

$$p = \frac{\lambda^{D_f}}{\lambda^{D}} = \lambda^{-c_f} \tag{14}$$

where $c_f = D - D_f$, the fractal co-dimension of the field. The fractal dimension D_f indicates how the binary field (rain and no rain in this case) fills the available space in a scale invariant way. As D is constant, in order to fully characterize the field a value of D_f for each threshold is required. This is the intuitive notion of multifractality. In order to be mathematically consistent, this characterization should actually be done with the help, not of a direct threshold at the maximum resolution, but with a scale-invariant threshold called singularity γ, and their corresponding codimension function $c(\gamma)$ as :

$$p\left(\varepsilon_\lambda \geq \lambda^{\gamma}\right) \approx \lambda^{-c(\gamma)} \tag{15}$$

Above equation implies that statistical moments q of the field scale with resolution (Schertzer and Lovejoy, 1987, 1988) are :

$$\langle {\varepsilon_\lambda}^q \rangle \approx \lambda^{K(q)} \tag{16}$$

where $K(q)$ is the moment scaling function related to $c(\gamma)$ by Legendre transform (Parisi and Frisch, 1985). For a conservative field in UM framework, $K_c(q)$ can be fully characterized with only two parameters, multi-fractality index α and mean intermittency codimension C_1.

$$K_c(q) = \frac{C_1}{\alpha - 1}\left(q^\alpha - q\right) \tag{17}$$

C_1 measures clustering of average intensity across scales; when the field is homogeneous C_1 is equal to zero. α measures how this clustering changes with respect to intensity levels; $\alpha \in [0,2]$. Larger values of both corresponds to stronger extremes. Simulations of such fields can be obtained by generating a levy noise with parameter α, 'coloring' it to introduce C_1 and then taking the exponential which yields solely non-negative values.

For a non conservative field ϕ_λ, i.e. a field whose average ($\langle \phi_\lambda \rangle$) changes with scales, a non-conservative parameter H is used in expression of scaling:

$$\phi_\lambda = \varepsilon_\lambda \lambda^{-H} \tag{18}$$

where ε is a conservative field characterized with C_1 and α.

Positive H represents a smoother field which needs to be fractionally differentiated for obtaining a conservative field. Conversely negative H represents a field in need of fractional integration for retrieving conservative field. H is related to the spectral slope β, which gives a measurement of the correlation range. Larger β means higher contribution of large-scale phenomenon in variability of data.

$$\beta = 1 + 2H - K_c(2) \tag{19}$$

315 *2.2.2. Estimation of scaling behaviour and UM parameters*

316 The quality of scaling of multifractal fields can be examined using trace moment (TM)
317 where log-log plot of upscaled fields against resolution λ is taken for each moment q (Eq.
318 16). For multifractal fields, the plot is a straight line with moment scaling function $K(q)$ as
319 slope. Quality of the scaling is given by the estimate R^2 of the linear regression. The value
320 for $q = 1.5$ is used as reference. Double trace moment (DTM) is a more robust version of
321 TM tailored for UM fields where the moment scaling function $K(q,\eta)$ of the field ${\varepsilon_\lambda}^{(\eta)}$
322 (obtained in practice by raising ε to power η at the maximum resolution and then upscaling
323 it) is expressed as a function of multifractality index α (Lavallée et al., 1993) :

$$\langle \left({\varepsilon_\lambda}^{(\eta)}\right)^q \rangle \approx \lambda^{K(q,\eta)} = \lambda^{\eta^\alpha K(q)} \tag{20}$$

324 From the above equation, value of α can be obtained as the slope of the linear part when
325 $K(q,\eta)$ is represented for a given q as a function of η in log-log plot.

326 *2.2.3. Power law relations in UM framework and practical implementation*

327 If a field is UM, then a power law relation of it is also a UM field with coefficients
328 depending upon initial UM parameters. The reasoning for power law comes from the DTM
329 analysis in UM framework (Tessier et al., 1993; Lovejoy et al., 2008).

330 Consider two multifractal fields (ε_1 and ε_2) that are power law related by an exponent
331 a and a prefactor b, as below :

$$\varepsilon_1 = b\varepsilon_2^a \tag{21}$$

From exponents in Eq. 20, $K(q)$ of ε_1 can be expressed as follows

$$\begin{array}{rcccl} <(\varepsilon_1)^q> & \approx & <(\varepsilon_2{}^{(a)})^q> & \approx & \lambda^{K_{\varepsilon_2}(q,a)} \\ K_{\varepsilon_1}(q) & = & K_{\varepsilon_2}(q,a) & = & a^{\alpha_{\varepsilon_2}} K_{\varepsilon_2}(q) \end{array} \tag{22}$$

Expanding $K(q)$ with UM parameters (as in Eq. 17)

$$\frac{C_{1,\varepsilon_1}}{\alpha_{\varepsilon_1}-1}(q^{\alpha_{\varepsilon_1}}-q) = a^{\alpha_{\varepsilon_2}} \frac{C_{1,\varepsilon_2}}{\alpha_{\varepsilon_2}-1}(q^{\alpha_{\varepsilon_2}}-q) \tag{23}$$

From above equation, we can deduce that for if a power relation exists, the UM parameters are related as follow :

$$\begin{aligned} \alpha_{\varepsilon_1} &= \alpha_{\varepsilon_2} = \alpha \\ C_{1,\varepsilon_1} &= a^{\alpha} C_{1,\varepsilon_2} \end{aligned} \tag{24}$$

In this study, both KE and R time series were analysed using UM framework. As the UM model discussed here is solely non negative, it removes all possibility of having non-negative values for both fields in analysis. Using their UM parameters in Eq. 24, it is possible to formulate power law relationship in the format of Eq. 21. It has the same shape as the theoretical power law obtained using moments of the DSD in section 2.1, in Eq. 11. Details of disdrometer data collection and subsequent multifractal analysis are covered in upcoming sections.

3. Data collection and instrumentation

3.1. Measurement campaigns

For this study, continuously monitored data in natural conditions was obtained from three optical disdrometers operating with two different principles. The devices are part of the TARANIS observatory (exTreme and multi-scAle RAiNdrop parIS observatory, Gires et al., 2018) of the Fresnel Platform of École des Ponts ParisTech (`https://hmco.enpc.fr/Page/Fresnel-Platform/en`); and are operated by Hydrology Meteorology and Complexity laboratory of École des Ponts ParisTech (HM&Co-ENPC). Table 1 gives a brief outline of measurement campaigns. From November 2016 to September 2017 the instruments were moved to École Polytechnique (EP) on SIRTA (Site Instrumenté de Recherche par Télédétection Atmosphérique) for a joint intensive measurement campaign over the Ile-de-France region. The aforementioned location is about 38 km away from ENPC towards south west of Paris. To summarise, the measurements presented in the following sections involve two different types of optical disdrometers and data collected from two different locations of Paris region.

Figure 1: Location of disdrometers in Paris area, at ENPC and EP SIRTA (basemap from openstreetmap.org)

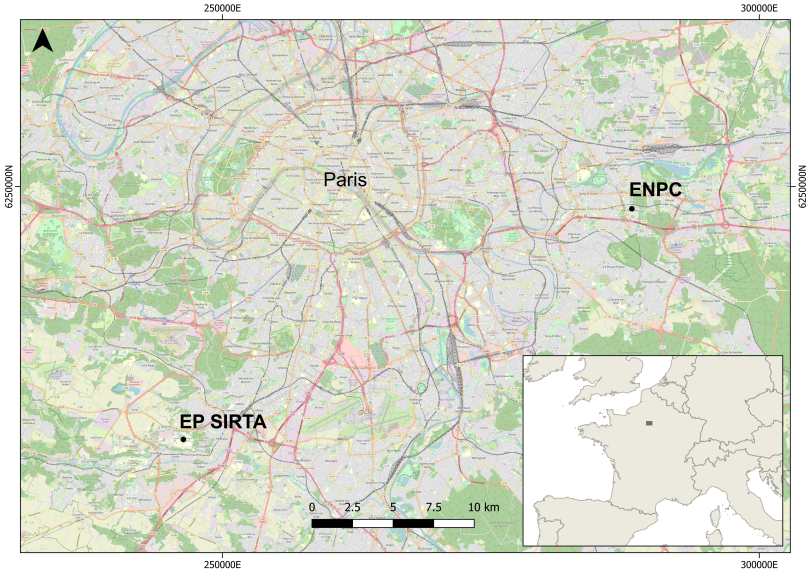

location	start time	end time
ENPC (1)	18 Jun 2013	10 Nov 2016
EP SIRTA	14 Nov 2016	20 Sep 2017
ENPC (2)	27 Dec 2017	31 Dec 2019

Table 1: Short description of the precipitation measurement campaign selected

3.2. Overview of instrument functioning and outputs

The three optical disdrometers used here are two OTT Parsivel^2 (see Battaglia et al., 2010 or the device documentation OTT, 2014) and one PWS 100 (see Ellis et al., 2006 or the device documentation Campbell-Scientific-Ltd, 2012).

The OTT Parsivel^2 are occlusion based devices with a transmitter that creates laser sheet and an intercepting receiver directly aligned with it. The size (equivolumic diameter) and fall velocity are assessed from changes (decrease in amplitude of intensity and duration of the decrease) in received laser intensity due to the passing of rainfall drops through a sampling area of 54 cm^2. An ellipsoidal shape model with a standard relation between the

axis ratio and the equivolumic diameter are assumed for drops in the process.

The PWS100 consists of a transmitter that generates four horizontal parallel laser sheets, and two receptors which are not aligned with the transmitter. The signal received by each receptor corresponds to the light refracted by drops and contains four consecutive peaks associated with each laser sheet. From the delay between those peaks, fall velocity and diameter of the drops are estimated. PWS100 has a sampling area of 40 cm^2. Computations assuming spherical shape of droplets are performed here with a later correction for oblateness before final result generation (Gires et al., 2017).

Both disdrometers have a collection time step of 30 s and provide main output as a matrix containing the number of drops ($n_{i,j}$) recorded during the time step Δt according to classes of equivolumic diameter (index i defined by a centre D_i and a width ΔD_i both expressed in mm) and fall velocity (index j and defined by a centre v_j and a width Δv_j, both expressed in ms^{-1}). For Parsivel^2 there are 32 classes of ΔD_i from 0.062 mm to 24.5 mm and Δv_j from 0.05 ms^{-1} to 20.8 ms^{-1}. And for PWS the same ranges from 0.05 to 27.2 (ΔD_i, mm) and 0.05 to 27.2 (Δv_j, ms^{-1}) in 34 classes. Width of diameter and velocity classes are not similar for all classes, as they are designed to be more and more refined towards smaller values.

From the raw matrix, the studied rainfall parameters - rain rate, drop size distribution and time specific kinetic energy were obtained using following expression for each time steps.

$$R = \frac{\pi}{6\Delta t} \sum_{i,j} \frac{n_{i,j} D_i^3}{S_{eff}(D_i)} \tag{25}$$

$$N(D_i) = \frac{1}{S_{eff}(D_i)\Delta D_i \Delta t} \sum_j \frac{n_{i,j}}{v_j} \tag{26}$$

$$KE = \frac{\rho_{wat}\pi}{6\Delta t} \sum_{i,j} \frac{n_{i,j} D_i^3 v_j^2}{S_{eff}(D_i)} \tag{27}$$

where $S_{eff}(D_i)$ is the sampling area of disdrometer in mm^2, Δt is the time step duration in hr and ρ_{wat} is the volumic mass of water ($10^3\,kg\,m^{-3}$). $N(D_i)\Delta D_i$ gives the number of drops with a diameter in the class i per unit volume (in m^{-3}). Details of the devices, their functioning and data collection can be found in Gires et al. (2018).

3.3. Data quality and filtering

For the data presented in this paper, filters suggested by various authors (Kruger and Krajewski, 2002; Thurai and Bringi, 2005; Jaffrain and Berne, 2012; Gires et al., 2018) were used to remove possible non-meteorological measurements (from environmental factors such as splashing, horizontal wind etc.) on the basis of size and velocity of drops. Using the disdrometer data set, two series of Multifractal analysis were performed - event based and year based. For event based analysis, individual rainfall events were identified with following criteria in rain intensity time series - rainfall events with a cumulative depth greater than 0.7 mm and separated by at least 15 minutes of dry weather before and after. From all measured events with this condition, rain rate (R), drop size distribution (DSD) and kinetic energy (KE) were calculated for the three disdrometers (denoted Pars 1, Pars 2 and PWS hereafter). From the results further filtering was done to remove events having a percentage of *nan* values (not a number - blank /missing data) > 1 % and R^2 value < 0.9, for both KE and R. Remaining *nan*s were then replaced with 0. In year based methodology, continuous time series from Jan 2016 to Dec 2019 - including rain and no rain conditions

- were used for multifractal analysis, and results were compiled according to the year of measurement.

There were minor lapses in continuity of data measurement from Jun 2013 to Dec 2015; for that reason those time periods were not considered in continuous year based analysis to avoid possible measurement biases. However, since selection of individual events are not affected by that, event based analysis involves data from Jun 2013 to Dec 2019. Lesser number of events can be observed in the excluded years for year based analysis in Table 2. Between 2016 and 2019, there were also a few days of maintenance where data was not recorded - 27 Sep 2017 to 26 Dec 2017, 01 to 07 Jan 2018 and 12 to 14 Apr 2019. After quality control for each disdrometer, a total of 214,665 time steps were analysed in 556 rain events (total 1610 events counting all three disdrometers; data was not always available for all the disdrometers, hence the lesser number) from 2013 to 2019 for event based analysis. In year based analysis, a total of 3,919,680 time steps were considered from 2016 to 2019; percentages of rainy time steps were about 7%, 6.6% and 5.7% for Pars 1, Pars 2 and PWS respectively.

4. Results and discussions

4.1. Overview of analysis

For analysing the KE and R time series using UM framework, as explained in previous sections, two strategies were followed - event based analysis and year based analysis. For event based analysis, we identified a total of 556 rainfall events between 28 Sep 2013 and 31 Dec 2019 of which 493 events were common among all three disdrometers. For UM analysis, each time series was resized to the highest power of two in such a way that the trimmed series accommodated maximum rainfall cumulative depth and then the field was

normalized. After resizing for UM analysis, length of individual events ranged from 64 to 2048 time steps, where each time step corresponds to 30 s, i.e. the recording time step of disdrometers used. KE and R from each events were analyzed as separate fields in UM framework. For year based methodology, similar procedure was followed for UM analysis on year long continuous time series, for the years from 2016 to 2019.

In coming subsections, estimation of UM parameters and power law relations are illustrated using one event data for event based analysis and one year data for year based analysis. Power law coefficients were also estimated using theoretical framework with DSD parameters as mentioned in section 2.1. Variation and correspondence among coefficients determined by UM and DSD parameters are discussed thereafter and validated with data.

4.2. Multifractal analysis of events

For illustration of the analysis carried out, one event from 2017 for Pars 1 disdrometer, that occurred on 16 September between 11:35:00 and 13:00:00 (local time) is presented here. Figure 2a displays the time series of R and KE for this event, as well as KE vs. R plots. The latter also shows power law fits with coefficients from UM analysis and DSD parameters (explained later in this section). For this event, 171 time steps were trimmed to 128 time steps along region of maximum rain occurrence of which 124 were rainy data points. Trimmed and normalized KE and R were then subjected to analysis using UM framework discussed in section 2.2. Initial analysis indicated values of non-conservative parameter H greater than 0.5 among many events. Hence to retrieve a conservative field on which the UM analysis can be implemented without bias, fluctuations of KE and R time series were used (Lavallée et al. 1993). Characterization of variability in KE field for the event considered here can be seen in Figure 2b with TM (Eq. 16 in log-log plot), DTM

graphs (Eq. 20 in log-log plot) and UM parameter values. As shown in TM and DTM graphs, the field exhibits a very good multifractal behaviour with a single scaling regime from 30 s to 64 min. For example, TM coefficient of determination r^2 for $q = 1.5$ was greater than 0.99. Values of UM parameters α, C_1, and H for KE of this particular event were 1.820, 0.311 and 0.547 respectively. It should be mentioned that H computed on the fluctuations of KE was found to be equal to 0.189, meaning the taking the fluctuations indeed enabled retrieval of a conservative field from the original smoother field. R also exhibited excellent scaling behavior and corresponding values of UM parameters α, C_1, and H for this event were 1.655, 0.229, and 0.100 respectively.

Figure 2: a) Time series of R, time series of KE, KE vs R graph b) and c) MF analysis graphs with KE and R (log-log plot of Eq. 16 and Eq. 20 for TM and DTM analysis respectively and log-log plot of exponents in Eq. 20 for UM parameters) for Pars 1 event 16 September 2017 11:35:00 to 13:00:00

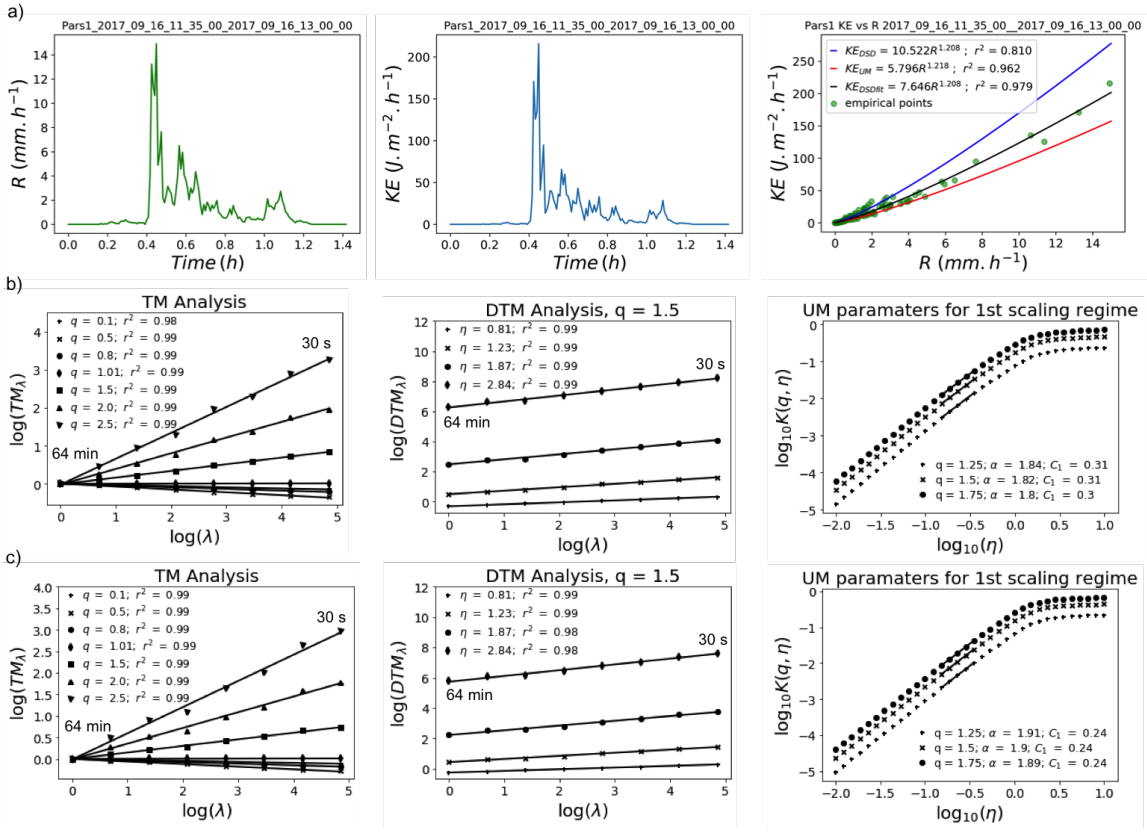

KE and R analyzed from every event exhibited similar multifractal characteristics with a unique scaling regime. The quality of scaling was examined using coefficient of determination, R^2 for $q = 1.5$ in TM analysis, and as previously mentioned events with values < 0.9 were discarded. 9.8 % percentage of total events were rejected on this basis. For the events with good scaling behaviour, robust retrieval of multifractal parameters α, C_1, β and H was possible. For example, the assessed values of α and C_1 for both KE and R time series, exhibited a maximum standard deviation (using various values of q in DTM analysis) of 0.0584 and 0.0670 for measurement at EP-SIRTA and 0.0446 and 0.0443 for

measurements at ENPC.

Figure 3 displays the values of multifractality index α and mean intermittency C_1 for all the studied events for both fields. It appears that the values of α for KE and R are rather well distributed along the bisector. This pattern suggests a power law relation between these two quantities as discussed in section 2.2 (Eq. 21) where ε_1 and ε_2 are KE and R respectively (i.e. $KE = bR^a$ as in Eq. 11). The exponent of the power law a was deduced from corresponding α and C_1 values of UM fields (KE and R) for every event subjected to UM analysis, using the expected relations for power law related UM fields, i.e. Eq. 24. The α used is the average of α_{KE} and α_R (which were anyway similar). Value of prefactor b was estimated by fitting Eq. 11 at maximum resolution with estimated values of a on event's $KE - R$ graph. For the event used as illustration, we found a = 1.083 and b = 11.493. This power law fit from UM parameters is displayed in Figure. 2a as KE_{UM} in the KE vs. R graph.

Variation of computed power law exponent a and prefactor b are also shown in Fig. 3 as time series of events for each year. Graphs of remaining years are provided in appendix A. For 3.5 % of total events filtered, estimates of α was found to be greater than the theoretical maximum (> 2); however a values for those events were found to be consistent with the overall average. Despite appreciable variability in UM parameters across events, values of a and b showed overall stability in the short range of values specified in graphs, suggesting robustness of the estimates. Year wise average values over the events for a and b, and number of events for all three disdrometers are given in Table 2. Average values of power law parameters from the events that were common between the three disdrometers are also shown in the same table. Comparable values of a and b were observed in both cases. A clear range of variation can be observed between the two types of disdrometers. For both

Parsivel^2 the average a and b were similar and around 1.22 and 8.17 respectively, while for PWS100 a values were consistently lower than that of Parsivel^2 at around 1.17 and b values greater at 13.02. PWS generally registered slightly higher intensities than Pars 1 and Pars 2. It should be mentioned that a and b seem to show a very rough correlation where values of b decreases with increase in values of a. But between make of instruments, irrespective of the type and number of events, values of a remains rather constant. Differences in values obtained between Parsivel^2 and PWS is expected due to operational differences between disdrometers. Such effects are also reported in Johannsen et al. (2020a) who showed biases in measurement and subsequent $R-KE$ relation due to difference in type of sensors used (three optical disdrometer were used). Angulo-Martínez and Barros (2015) also highlighted some differences among various Parsivel^2.

Figure 3: Year wise α and C_1 variation on event based analysis from 2016 to 2019 (remaining years are provided in appendix)

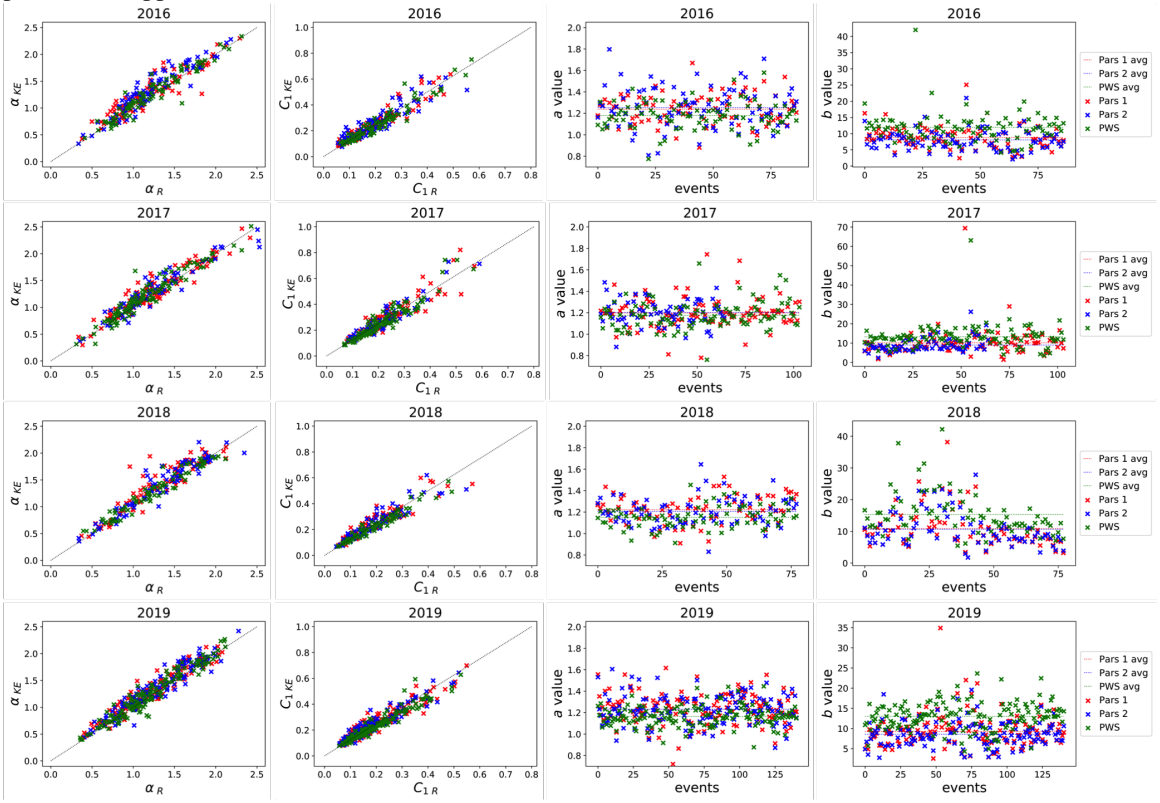

year	location	disdrometer	total events			common events		
			# events	avg a	avg b	# events	avg a	avg b
2013	ENPC	Pars 1	29	1.248	9.224	11	1.246	9.224
		Pars 2	11	1.254	9.093		1.254	9.093
		PWS	29	1.186	11.912		1.193	11.748
2014	ENPC	Pars 1	84	1.207	11.548	84	1.207	11.548
		Pars 2	84	1.186	11.065		1.186	11.065
		PWS	84	1.159	14.065		1.159	14.065
2015	ENPC	Pars 1	38	1.235	9.459	38	1.235	9.459
		Pars 2	38	1.207	8.532		1.207	8.532
		PWS	38	1.190	11.712		1.190	11.712
2016	ENPC	Pars 1	87	1.238	8.802	87	1.238	8.802
		Pars 2	87	1.253	8.069		1.253	8.069
		PWS	87	1.180	11.939		1.180	11.939
2017	EP-SIRTA*	Pars 1	102	1.197	10.126	65	1.193	10.013
		Pars 2	65	1.202	8.944		1.202	8.944
		PWS	104	1.176	13.238		1.151	15.282
2018	ENPC	Pars 1	78	1.221	10.832	78	1.221	10.832
		Pars 2	78	1.205	10.647		1.205	10.647
		PWS	78	1.151	15.282		1.151	15.282
2019	ENPC	Pars 1	138	1.231	9.254	130	1.238	8.913
		Pars 2	130	1.231	8.550		1.231	8.55
		PWS	141	1.165	13.024		1.649	12.960

Table 2: a, b and no. of events analysed between 2013 and 2019 according to location of measurement and disdrometer used.
* From Nov 2016 to Sep 2017 as shown in Table 1; preceding and succeeding years are adjusted accordingly, refer Table 1.

4.3. Multifractal analysis of continuous data (year based analysis)

To illustrate year based analysis, continuous time series and UM analysis for Pars 1 disdrometer for the year 2017 is shown in Fig. 4. Both KE and R fields showed similar multifractal features. Scaling behaviour of KE is shown in Fig. 4b. A unique scaling regime from 30 s to 311 days was considered.

Figure 4: a) Time series of R, time series of KE, KE vs R graph b) and c) Multifractal analysis graphs with KE and R (log-log plot of Eq. 16 and Eq. 20 for TM and DTM analysis respectively and log-log plot of exponents in Eq. 20 for UM parameters) using the year based analysis, for Pars 1, for 2017

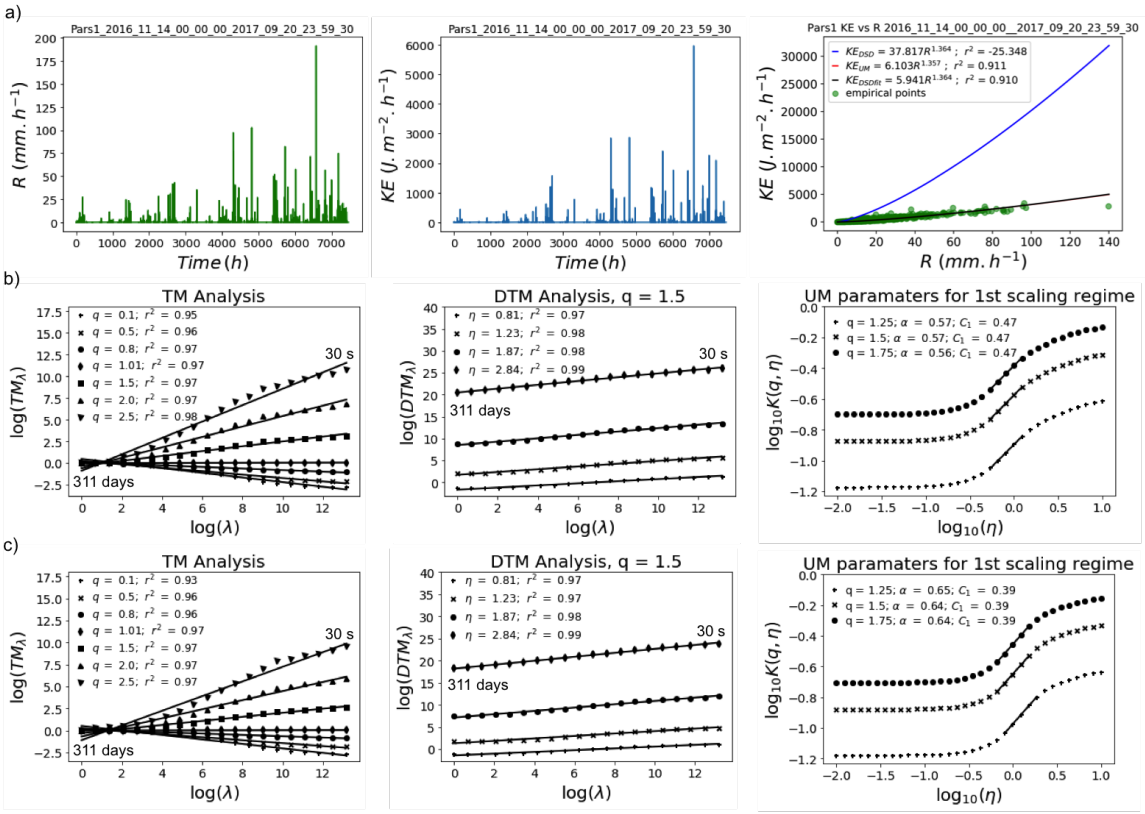

Variation of UM parameters α and C_1 between KE and R fields as well as values of power law exponent a and prefactor b (computed by fitting the relation at maximum resolution) are displayed in Fig. 5. Precise values of a and b according to the year of measurement are given in Table 3 in annexes. The curve KE_{UM} in the KE vs R graph of Fig. 4a, shows the power law fit using UM parameters for continuous data of 2016, for Pars 1. Values and trend of variation are similar to that observed for the event based analysis. This confirms the robustness of the discussed power law, which is valid and retrieved not only at the event scale, but also at the year scale.

Figure 5: a) Results from multifractal analysis on continuous year wise data set: a) α and C_1 (DTM); b) a and b values

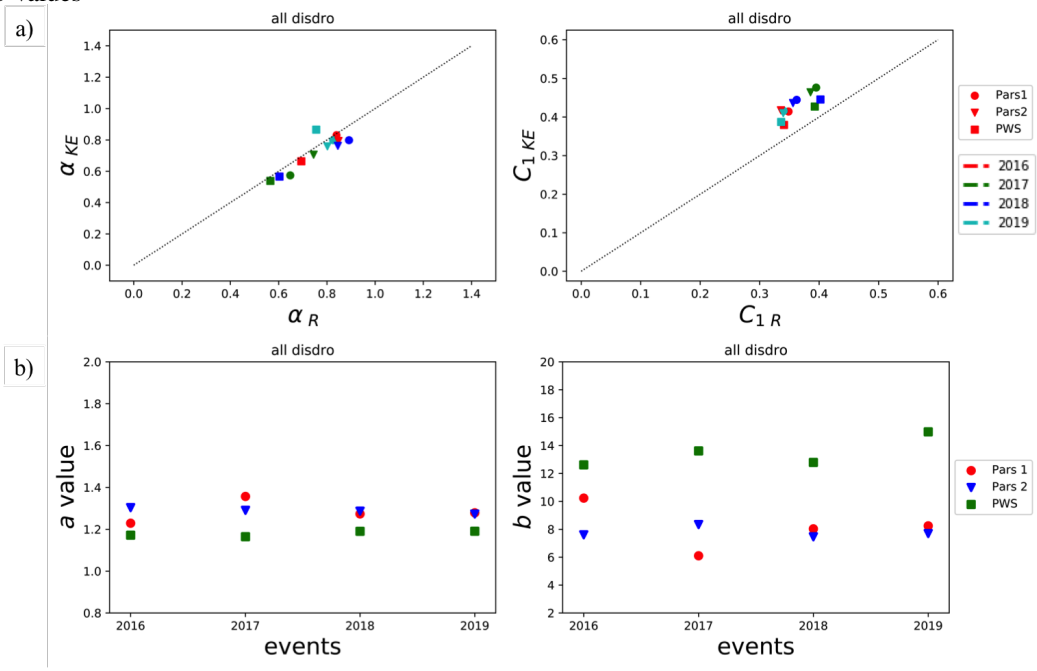

Disdrometer	coefficient	2016	2017*	2018	2019
Pars 1	a	1.229	1.356	1.273	1.278
	b	10.232	6.102	8.033	8.247
Pars 2	a	1.303	1.290	1.286	1.273
	b	7.605	8.338	7.463	7.695
PWS	a	1.171	1.164	1.190	1.190
	b	12.616	13.614	12.792	14.981

Table 3: a and b from year based analysis, from 2014 to 2019 according to disdrometer used for measurement.
* From Nov 2016 to Sep 2017 as shown in Table 1; preceding and succeeding years are adjusted accordingly

4.4. Power law coefficients from DSD parameters

To understand previous findings further, values of a and b were computed from theoretical framework discussed in section 2.1. Rainfall DSD was assumed to follow gamma distribution (Eq. 3) and theoretical values of a and b (denoted as a_{DSD} and b_{DSD} from here

on for clarity) were computed as per Eq. 12 after estimating values of gamma DSD parameters (μ, N_0 and Λ) with the help of method of moments. The variation of rain rate R was accurately reproduced using M234 moment estimators (Fig. 8d for example). Theoretical power law relation ($KE_{DSD} = b_{DSD}R^{a_{DSD}}$) was then compared with the one estimated using UM analysis (represented from here on as KE_{UM} with coefficients a_{UM} and b_{UM} for clarity) for every events. Average values of DSD parameters, estimation error and corresponding a_{DSD} and b_{DSD} for Pars 1 events are given in Table 4 according to event's rain type (definition introduced later). $RMSE_{DSD}$ is the root mean square error (RMSE) between empirical DSD and theoretical gamma DSD with fitted parameters (using the value for the center of each diameter class D_i). It is used here as an indicator of the quality of fit of the assumed gamma DSD distribution and the empirical one. For $RMSE$ estimation only the portion of DSD above 0.5 mm diameter class was considered as smaller drops have lesser contribution in overall KE and R, and are associated with greater uncertainties in measurement. Also, higher size drops (above 9 mm diameter class) were not observed during the events and are hence not shown in DSD figures discussed after (Fig. 6 and Fig. 8).

Figure 6:
a) 2019 Pars 1 event where empirical DSD corresponds with gamma distribution and b) where it doesn't follow gamma distribution (DSD displayed only till diameter class around 9 mm as higher drops were not observed during the events)

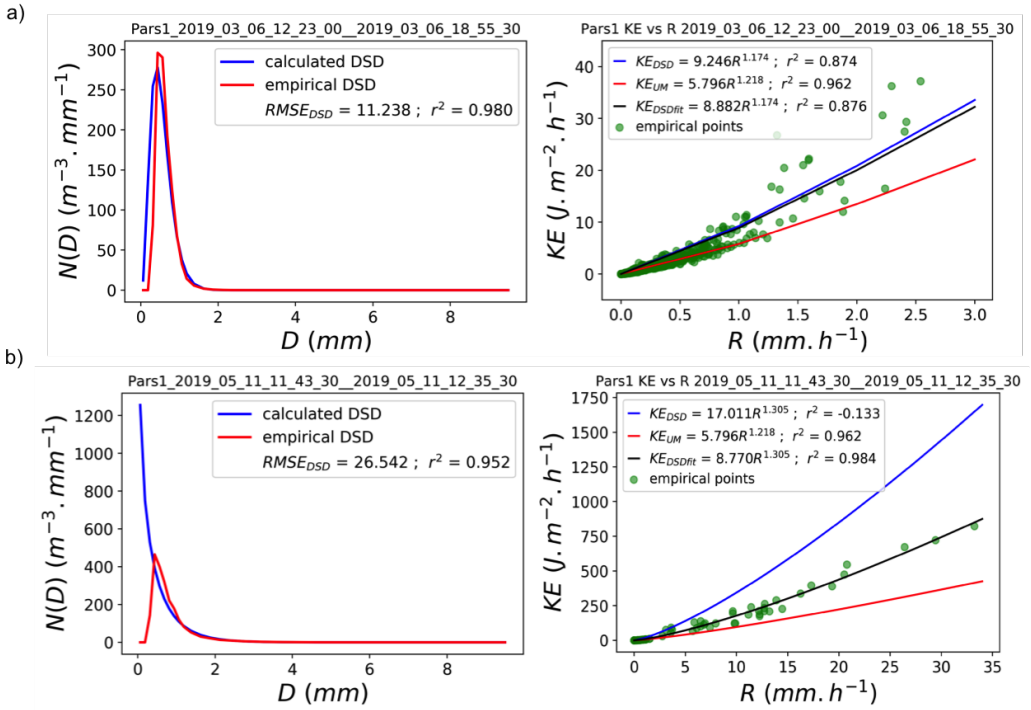

Figure 6 represents two extremes cases among events from year 2019 for Pars 1: one event (Fig. 6a) where empirical DSD corresponds with a gamma distribution and one event (Fig. 6b) where it does not. The DSD fitting as well as the KE vs. R plots (fitted with power law relation from UM analysis and DSD extraction) are also displayed. For the event with empirical DSD closer to estimated gamma DSD, both power law relations (KE_{UM} & KE_{DSD}) are similar and show good fit. For the other event, power law relation from DSD approach shows a considerable deviation from actual values of KE, with a strong overestimation. Power law from UM analysis on the other hand still provides a close fit. To see if there is such a trend through all the events, coefficient of determination of both $KE - R$ fits were plotted against each other (r^2_{UM} vs r^2_{DSD}) and compared using corresponding

values of $RMSE_{DSD}$ (Fig. 7a). Negative value of coefficient of determination for DSD ($r^2_{DSD)}$) is due to the high difference between KE_{DSD} and empirical KE in certain events. From the plot it is evident that a generalized conclusion - theoretical values of a and b (a_{DSD} & b_{DSD}) works well in cases where empirical DSD coincides with gamma DSD - is not possible. However, there were many events with good DSD correspondence with gamma, where KE_{DSD} fitted data better.

Figure 7:
a) r^2 values between KE_{UM} and KE_{DSD} for Pars1, 2019; b) r^2 values between KE_{UM} and KE_{DSDfit} (b from fitting of data) for Pars1, 2019 (RMSE calculated by considering only parts of DSD where drop diameter > 0.5 mm)

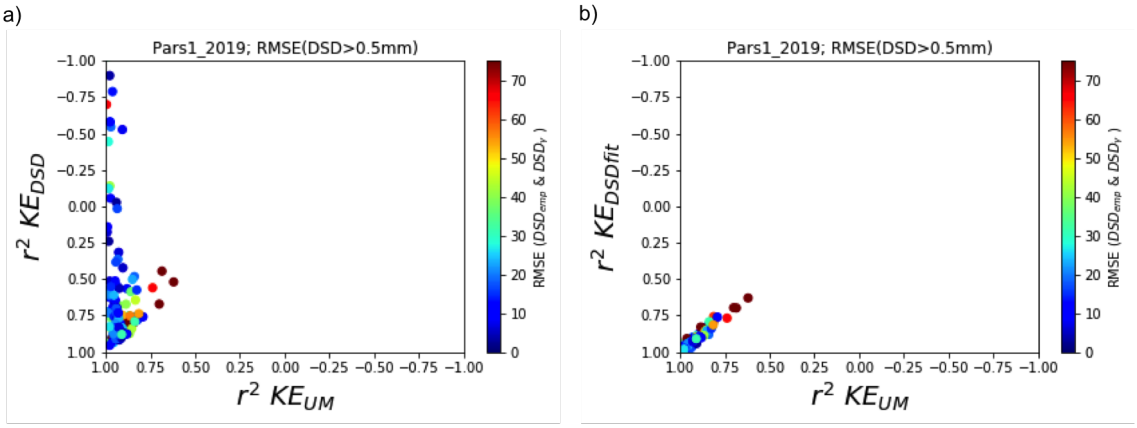

To investigate further this issue and given that the DSD is available for all time steps, a_{DSD} and b_{DSD} were computed for each time step to study their variations within a rainfall event. Figure 8 displays their temporal evolution for the event in Fig. 2. Values of parameters, especially b_{DSD}, shows considerable variation within an event. These variations basically come from variations in DSD parameters μ an N_0 as it can be seen on Fig. 8c and 8f (also evident from Eq. 12), which are reflecting physical variations in the rainfall process. It should be mentioned that during this event (and other events), gamma DSD parameters were able to properly reproduce observed rain rate (Fig. 8d), meaning that the

assumption of gamma DSD distribution and the M234 moment estimator approach remains valid throughout the event(s). This suggests that the variability of a_{DSD} and b_{DSD} observed at event scale is also valid within events at much smaller scales. This could explain some of the bias previously observed with DSD approach developed in this paper.

As there were still considerable variation in r^2 values of $r^2_{KE_{DSD}}$ (Fig. 7a), especially if we compare with KE_{UM} which shows better $r^2_{KE_{UM}}$ regardless the type of event, a question of possible bias arises due to difference in methods of estimation of power law coefficients. Unlike KE_{DSD} for which both coefficients are obtained from theoretical relation involving DSD parameters, for KE_{UM} only coefficient a is fully estimated from UM analysis. Prefactor b_{UM} is obtained by fitting the data at highest available resolution (30 s) using UM estimated a_{UM}. Such discrepency may introduce a bias in the comparison between DSD and UM approach to retrieving a power law. Hence, to understand this further and to make a fair comparison, a new power law was considered where only a_{DSD} is obtained using Eq. 12 while b_{DSD} is calculated from fitting of data (denoted hereafter b_{DSDfit}) - KE_{DSDfit}. Figure 7b shows r^2 between KE_{DSDfit} and KE_{UM}; and it can be seen that comparable fits are obtained between UM and DSD power laws regardless the nature of DSD, thus illustrating the presence of bias. This can also be observed in previous $KE - R$ plots - Fig. 2a, Fig. 4a, Fig. 6a and Fig. 6b.

Figure 8: Variation of a_{DSD} and b_{DSD} for each time steps in an event (same event discussed in Fig. 2)
a) Correspondence between empirical DSD (red) and calculated DSD (blue); d) Correspondence between empirical rainfall rate (R_{emp}) and that calculated from DSD moments (R_{DSD})
b) & e) Variation of a_{DSD} and b_{DSD} within the event
c) & f) Variation of a_{DSD} and b_{DSD} with DSD parameters N_0 and μ

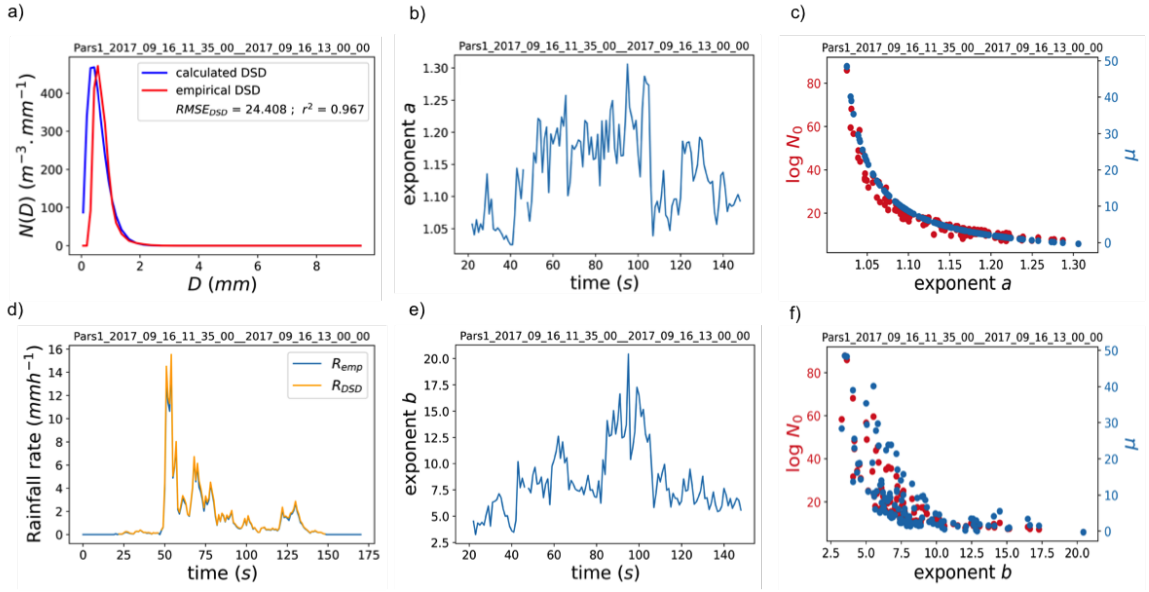

4.5. *Comparison between $KE - R$ relations*

Though the power law obtained is similar from UM and DSD analysis, they fit the data differently due to difference in values of corresponding parameters. KE_{DSD} in KE vs. R graph of Fig. 2a and Fig. 4a shows the power law fit using theoretical a and b (a_{DSD} & b_{DSD}), from DSD parameters for illustrated examples in event based and year based analysis analysis. The difference in fit between two calculations of power law, KE_{UM} and KE_{DSD} can be observed there. It can be seen from Fig. 7a that KE_{UM} gives rather good fit regardless the event specific DSD shape, while r^2 value of KE_{DSD} fluctuates. However, there is a limited tendency for good fit towards empirical DSD following gamma distribution (for few events like Fig. 6). Figure 9 shows variation of a and b estimates from DSD and UM for Pars 1, Pars 2 and PWS for all events in year 2019. Values of a_{UM} and a_{DSD}

are mostly clustered around the approx. 1.2 for all three disdrometers with no clear relation between them. On the other hand, values of b_{UM} and b_{DSD} are more spread out, ranging approximately from 2 to 25. Such spreading for b_{DSD} is not caused by the computation issues previously mentioned since it is visible on both b_{DSD} and b_{DSDfit}. This observed scattering, which is comparable regardless the estimation techniques and device, suggests that even if the power relation between KE and R remains relevant for all events, its parameters exhibit strong variability between events.

Figure 9: Variation of power law coefficients from UM and DSD calculation, for events in year 2019 (similar variation for other years also)

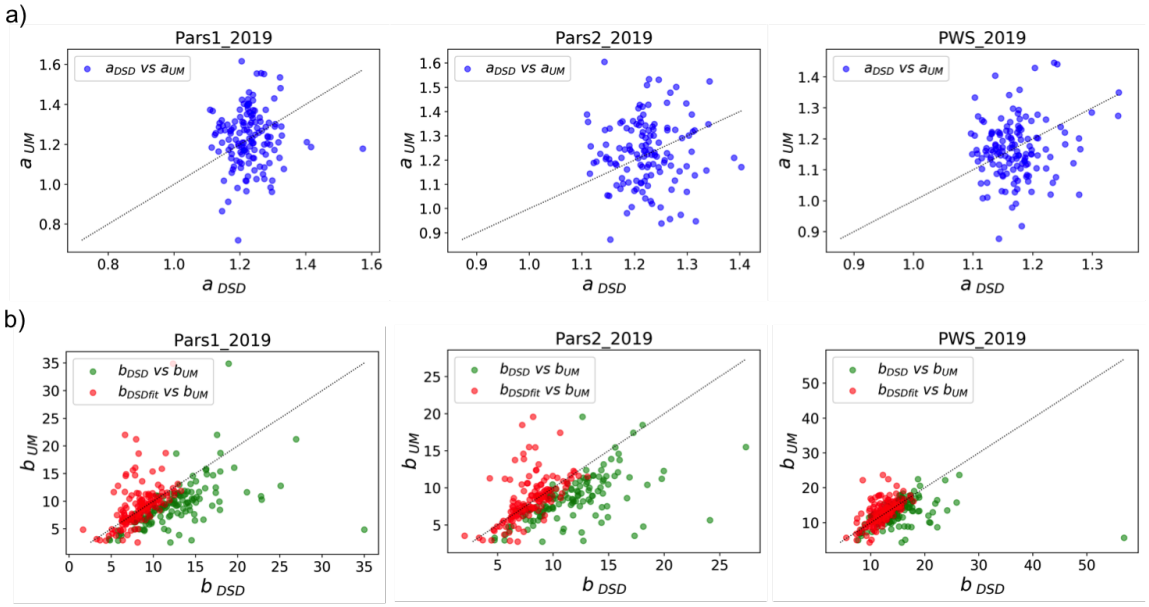

The constants of the power law relations (in literature) between KE and R are not universal in application and need tweaking as per the rainfall type, measurement location as well as techniques. Based on assumed dependence between DSD parameters and rain rate in formulation exponents; Salles et al. (2002) suggest four range of values for exponent values of the universal power law, and Uijlenhoet and Stricker (1999) propose six differ-

ent relationships in their research. Hence, in order to refine the analysis of this observed variability between events and to examine possible dependence of a and b on type of rain, events were sorted according to rain types. Table 4 shows, for Pars 1, averaged values of gamma DSD parameters, indicator of the quality of the fitting, and power law coefficients from both DSD and UM estimations across events sorted according to type of rainfall. Tables for Pars 2 and PWS are given in appendix - (Table B1). For defining types of rainfall from light to extreme, a classification based on intensity (Tokay and Short, 1996) was employed. μ, λ and N_0 tend to decrease with heavier events, with a stronger trend for N_0. It should be mentioned that an opposite trend is reported in reference used; this could be due to instrumental bias in DSD measurement as the impact disdrometer used in reference is known to under-represents smaller drops in intense rainfall. It should also be noticed that the capacity of the gamma distribution to model observed DSD diminishes with heavier rainfall (this is more visible on RMSE estimation over whole range of DSD and less prominent in displayed estimate here involving only higher drop sizes), suggesting a limit in validity for gamma distribution assumption. Also, an increase in mean diameter is noticed (not shown here). These findings are in agreement with previous studies reported in literature (Carollo Francesco Giuseppe and Ferro Vito, 2015). When it comes to power law coefficients, both a_{DSD} and b_{DSD} show increase with increasing rain rate, and this is more pronounced for b_{DSD}. Given the observed decrease in validity of gamma distribution of DSD, these trends should be taken carefully because they are likely to be mere artifacts and not representative of the actual process at stake. In the case of UM estimated parameters, b_{UM} follows similar trend with stronger magnitude (going from 8 to 33) while a_{UM} shows slight reduction in value with increasing rain rate (from 1.25 to 1.05). Since the average rainfall criteria used for classification here is a somehow arbitrary and more biased towards

lesser rainfalls, another classification relying on the maximum of 10 minute moving average was also employed. The results are tabulated in Table B2 (Appendix B). With this criteria which is more biased towards larger rainfall events, consistent and similar results are retrieved when it comes to values and variation of power law coefficients a and b, from DSD as well as UM, suggesting robustness of obtained trends.

		from DSD moments							**from UM**	
		# events	μ	N_0	Λ	**RMSE**$_{DSD}$	a_{DSD}	b_{DSD}	a_{UM}	b_{UM}
				$(m^{-3}mm^{-1-\mu})$	(mm^{-1})	$(m^{-3}mm^{-1})$		$(Jm^{-2}mm^{-a}h^{a-1})$		$(Jm^{-2}mm^{-a}h^{a-1})$
very light	$R < 1$	188	2.53	1.05×10^7	6.34	19.32	1.196	11.056	1.253	8.554
light	$1 \leq R < 2$	173	1.75	1.71×10^9	4.81	24.53	1.222	12.694	1.224	9.334
moderate	$2 \leq R < 5$	141	1.01	2.51×10^7	3.42	21.25	1.256	15.580	1.214	10.216
heavy	$5 \leq R < 10$	36	0.44	1.40×10^4	2.25	20.45	1.275	17.259	1.210	11.336
very heavy	$10 \leq R < 20$	14	-0.05	1.17×10^3	1.63	21.14	1.300	18.419	1.119	19.670
extreme	$R \geq 20$	4	-0.85	5.48×10^2	1.04	44.82	1.353	44.82	1.052	33.250

Table 4: Variation of DSD parameters and power law coefficients according to the type of rainfall for Pars 1 (R = average rain rate for rainy time steps)

To evaluate the performance of established power law relationship across scales of measurement, KE was calculated from empirical R using $KE = bR^a$ with average values of a and b and compared with existing relations in literature. For this purpose, exponential equation used in RUSLE ($KE_{BF} = 29[1 - 0.72\exp(-0.05R)]$, Brown and Foster, 1987), exponential equation used in RUSLE2 ($KE_{MG} = 29[1 - 0.72\exp(-0.082R)]$, C. McGregor et al., 1995), universal exponential law proposed by van Dijk et al. (2002) ($KE_{VD} = 28.3[1 - 0.52\exp(-0.0421R)]$) and ideal power law proposed by Shin et al. (2016) ($KE_{Shin} = 10.3R^{11/9}$) were used alongside KE_{UM} and KE_{DSD} derived here (power law where fitted values of b were used -KE_{DSDfit}- is also included). For UM and DSD power laws in this paper, average values among all calculated events were used for representation according to make of disdrometers. Average values of coefficient a and prefactor b were close for both Pars 1 and Pars 2 disdrometers and were taken common for the

Parsivel^2 make (for both UM and DSD). It is also logical to keep values of power law coefficients separate between different disdrometers as varying KE and R estimation has been reported across types of disdrometers used (Angulo-Martínez and Barros, 2015; Angulo-Martínez et al., 2018; Johannsen et al., 2020b). Figure 10 shows KE and R variation fitted with above mentioned equations for maximum resolution, 30 seconds. As expected KE_{UM} provides better fit than KE_{DSD} (and KE_{DSDfit} shows closer fits). With respect to empirical data, UM power laws exhibit - for all three devices - slightly better or comparable coefficient of determination (r^2) with regards to commonly used relations. The exponential equations from literature appear very close to each other. The relatively lower values of coefficient of determination than that during event based fits are likely to be due to the effect of using average values instead of event specific values of a and b.

Figure 10: Fitting of empirical $KE - R$ using power laws from UM and DSD, and popular expressions from literature for a) and b) Parsivel^2, and c) PWS

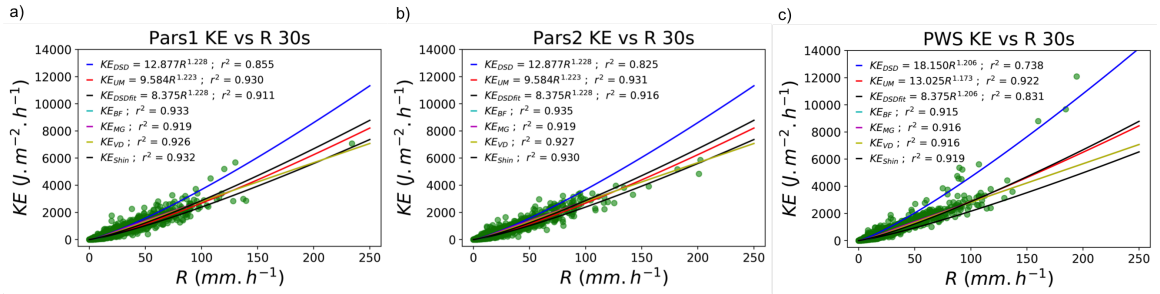

To understand the performance of various equations further, r^2 was examined across various time periods and also across different type of rains. Results are displayed in Fig. 11. It appears that regardless of the duration as well as type of rainfall considered, tuned relations KE_{DSDfit} and KE_{UM} perform significantly better than the other fixed ones, yielding r^2 values greater than 0.9. In most cases, KE_{UM} exhibits slightly better performances with a difference not significant. The analysis also confirmed the poor performance of KE_{DSD},

i.e. the inability of the DSD approach to properly fit the prefactor 'b'. It should be stated that the power law obtained using UM analysis is not providing significant performance enhancement compared to that obtained from gamma DSD while the prefactor b is estimated from fitting of the data (KE_{DSDfit}). However, with UM analysis, it is possible to discard all assumptions of DSD following a gamma distribution thus eliminating the known inadequacy of gamma model and its sensitivity to sampling resolution (Adirosi et al., 2013, 2014; Ignaccolo and De Michele, 2014; Adirosi et al., 2016; Gatidis et al., 2020). The inadequacy was observed in current analysis as well, as previously discussed and illustrated in Fig. 6 and Fig. 7.

Figure 11: r^2 values of various KE-R relations discussed for a) events analysed in 2017, 2018 and 2019 (for Pars 1),
b) all events grouped according to type of rain - light, moderate and heavy
Average value for each year is given in legends, with KE_{UM} and KE_{DSDfit} displayed in dotted lines

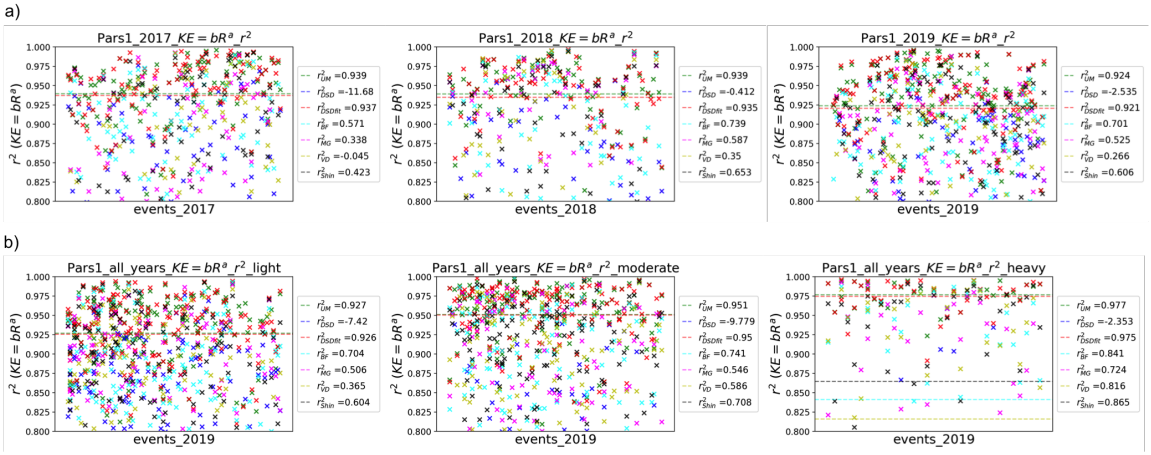

5. Conclusion

We examined the relationship between rainfall intensity R and time specific kinetic energy KE using high resolution (30 s) optical disdrometer data from the past 7 years in Paris region. The variability across scales of both parameters was characterized using the

framework of Universal Multifractals. Analyzed KE and R times series were found to convey excellent multifractal behaviour (which is novel for KE), with multifractality index α and mean intermittency C_1 suggesting power law relation between them; it can be written as $KE = bR^a$. Such power law was found to be valid across analyzed data, i.e. independent of the event, on whether they are computed on event or yearly basis, and of the underlying corresponding drop size distribution. Some variability in the value of the exponent a and prefactor b is reported according the event and disdrometer type.

As shown by previous results, similar power-law can be theoretically obtained when relying on the common assumption of a gamma distribution for the DSD, and a power-law relation between fall velocity and equivolumic drop diameter. KE-R relation obtained through UM analysis was compared with results found using this common framework and biases were acknowledged. Despite some exceptions, in most cases when a gamma DSD approximation was relevant, estimations of power law parameters from the two approaches were found to be consistent. When not, UM approach provided slightly better fit in general but not in a significant manner, keeping in mind that the pre-factor needs to fitted to data in both cases to ensure a fair comparison. Thus, the newly discussed power law relationship between KE and R retrieved with the help of UM framework generalizes previous results and theoretical formulations without having to rely on the ad-hoc assumption of a gamma DSD. The main underlying assumption of UM framework, i.e. that there is an underlying multiplicative process, is actually physically based in the sense that comes from the scale invariance features of the Navier-Stockes equations. Here, a UM analysis confirmed the validity of this assumption. Deriving the power-law relation in a multifractal framework opens the path to new approaches for simulating KE from simple R measurements. Given that complete KE measurement is much less available than R one, this impact will be

investigated further in future work.

For the future, it would hence be interesting to expand the data set across geographical and meteorological conditions to reduce the biases that might have accumulated from region of measurement.

Acknowledgements

The authors greatly acknowledge partial financial support from the Chair of Hydrology for Resilient Cities (endowed by Veolia) of the École des Ponts ParisTech, EU NEW INTERREG IV RainGain Project, EU Climate KIC Blue Green Dream project, the Île-de-France region RadX@IdF Project, and the ANR JCJC RW-Turb project (ANR-19-CE05-0022-01)

Appendix A: Multifractal events year wise

Figure A1: Year wise α and C_1 variation on event based analysis 2013 to 2015

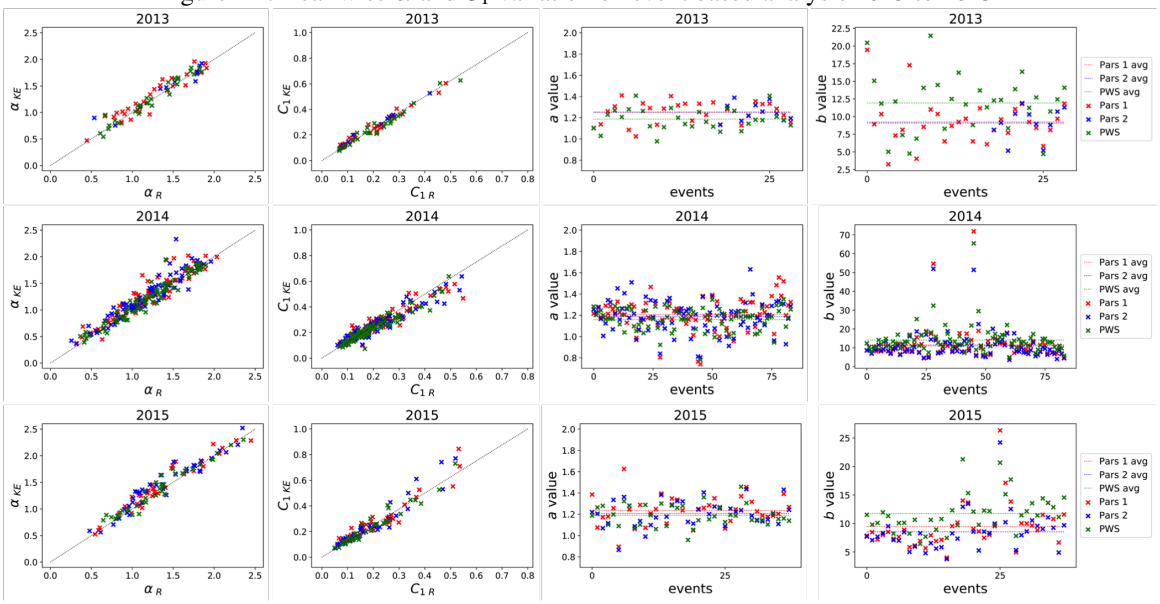

Appendix B: Method of moments

The formulation of moment estimator

Gamma distribution parameters were estimated from second, fourth and sixth moments using following relations:

M234:

$$D_m = M_4/M_3 \tag{B.1}$$

$$\eta = \frac{(M_3^2)}{(M_2 M_4)} \tag{B.2}$$

$$\mu = \frac{1}{(1-\eta-1)} - 4 \tag{B.3}$$

$$\Lambda = \frac{M_2}{M_3}(\mu+3) \tag{B.4}$$

$$N_0 = \frac{M_2 \Lambda^{(\mu+3)}}{\Gamma(\mu+4)} \tag{B.5}$$

DSD parameters and power-law coefficients

			from DSD moments						from UM	
		# events	μ	N_0	Λ	**RMSE**$_{DSD}$	a_{DSD}	b_{DSD}	a_{UM}	b_{UM}
				$(m^{-3}mm^{-1-\mu})$	(mm^{-1})	$(m^{-3}mm^{-1})$		$(Jm^{-2}mm^{-a}h^{a-1})$		$(Jm^{-2}mm^{-a}h^{a-1})$
Pars 2	very light $R<1$	190	2.53	1.36×10^{7}	6.59	19.78	1.196	10.180	1.246	8.097
	light $1\le R<2$	160	1.61	1.20×10^{8}	4.70	24.81	1.229	12.630	1.202	9.262
	moderate $2\le R<5$	101	0.82	1.66×10^{6}	3.19	20.93	1.260	15.026	1.208	9.911
	heavy $5\le R<10$	28	0.26	2.72×10^{4}	2.14	23.85	1.281	17.171	1.247	10.140
	very heavy $10\le R<20$	8	-0.38	5.81×10^{2}	1.36	21.20	1.317	19.951	1.098	19.997
	extreme $R\ge20$	6	-0.94	6.16×10^{2}	1.07	57.99	1.363	15.593	1.180	19.040
PWS	very light $R<1$	163	2.79	7.82×10^{6}	4.73	10.95	1.187	10.95	1.194	12.070
	light $1\le R<2$	176	2.65	2.64×10^{7}	4.15	14.30	1.195	14.30	1.154	12.703
	moderate $2\le R<5$	152	1.87	4.73×10^{3}	2.85	14.98	1.216	20.024	1.169	13.136
	heavy $5\le R<10$	46	1.16	2.82×10^{3}	1.96	18.90	1.253	24.439	1.193	13.933
	very heavy $10\le R<20$	18	0.59	7.07×10^{2}	1.51	19.24	1.266	20.834	1.133	18.983
	extreme $R\ge20$	6	0.53	4.09×10^{2}	1.28	20.63	1.26	21.031	1.165	18.016

Table B1: Variation of DSD parameters and power law coefficients according to the type of rainfall (R = average of rainy data points)

			from DSD moments						from UM	
		# events	μ	N_0	Λ	**RMSE**$_{DSD}$	a_{DSD}	b_{DSD}	a_{UM}	b_{UM}
				$(m^{-3}mm^{-1-\mu})$	(mm^{-1})	$(m^{-3}mm^{-1})$		$(Jm^{-2}mm^{-a}h^{a-1})$		$(Jm^{-2}mm^{-a}h^{a-1})$
Pars 1	very light $R<1$	13	3.82	1.30×10^{7}	8.19	8.19	1.161	9.471	1.245	8.396
	light $1\le R<2$	82	2.63	7.76×10^{6}	6.39	15.96	1.191	10.962	1.271	8.747
	moderate $2\le R<5$	235	2.04	1.10×10^{5}	5.32	21.77	1.213	12.528	1.227	9.119
	heavy $5\le R<10$	134	1.44	2.22×10^{7}	4.19	24.79	1.235	13.826	1.225	9.369
	very heavy $10\le R<20$	54	0.51	4.55×10^{3}	2.67	20.75	1.269	16.214	1.197	11.697
	extreme $R\ge20$	38	-0.22	1.77×10^{3}	1.67	26.84	1.314	26.84	1.147	16.642
Pars 2	very light $R<1$	13	4.27	2.02×10^{7}	8.94	6.75	1.154	9.097	1.217	7.833
	light $1\le R<2$	82	2.97	2.96×10^{6}	7.04	15.74	1.183	10.165	1.253	8.245
	moderate $2\le R<5$	215	1.99	9.38×10^{7}	5.43	22.15	1.214	11.857	1.212	8.810
	heavy $5\le R<10$	112	1.17	3.20×10^{6}	3.94	24.33	1.239	12.969	1.222	9.280
	very heavy $10\le R<20$	42	0.39	5.92×10^{3}	2.74	25.49	1.276	15.369	1.196	10.696
	extreme $R\ge20$	29	-0.63	1.78×10^{3}	1.55	35.88	1.343	18.133	1.192	13.445
PWS	very light $R<1$	6	3.84	3.39×10^{4}	6.15	6.78	1.16	13.92	1.223	13.322
	light $1\le R<2$	61	3.26	5.29×10^{4}	5.27	10.13	1.175	14.687	1.187	11.997
	moderate $2\le R<5$	201	2.59	1.91×10^{7}	4.20	12.56	1.195	17.258	1.176	12.602
	heavy $5\le R<10$	168	2.32	2.78×10^{6}	3.50	14.65	1.202	19.013	1.168	12.702
	very heavy $10\le R<20$	75	1.72	3.31×10^{3}	2.65	16.90	1.223	20.846	1.155	14.401
	extreme $R\ge20$	50	0.67	1.11×10^{3}	1.69	19.48	1.264	20.879	1.156	15.430

Table B2: Variation of DSD parameters and power law coefficients according to the type of rainfall (R = maximum value of 10 minute moving average)

References

Adirosi, E., Baldini, L., Lombardo, F., Russo, F., Napolitano, F., 2013. Comparison of different fittings of experimental dsd. AIP Conference Proceedings 1558, 1669–1672. URL: https://aip.scitation.org/doi/abs/10.1063/1.4825850, doi:10.1063/1.4825850, arXiv:https://aip.scitation.org/doi/pdf/10.1063/1.4825850.

Adirosi, E., Gorgucci, E., Baldini, L., Tokay, A., 2014. Evaluation of Gamma Raindrop Size Distribution Assumption through Comparison of Rain Rates of Measured and Radar-Equivalent Gamma DSD. Journal of Applied Meteorology and Climatology 53, 1618–1635. URL: http://journals.ametsoc.org/doi/10.1175/JAMC-D-13-0150.1, doi:10.1175/JAMC-D-13-0150.1.

Adirosi, E., Volpi, E., Lombardo, F., Baldini, L., 2016. Raindrop size distribution: Fitting performance of common theoretical models. Advances in Water Resources 96, 290–305. URL: http://www.sciencedirect.com/science/article/pii/S0309170816302639, doi:10.1016/j.advwatres.2016.07.010.

Angulo-Martínez, M., Beguería, S., Latorre, B., Fernández-Raga, M., 2018. Comparison of precipitation measurements by ott parsivel^2 and thies lpm optical disdrometers. Hydrology and Earth System Sciences 22, 2811–2837. URL: https://www.hydrol-earth-syst-sci.net/22/2811/2018/, doi:10.5194/hess-22-2811-2018.

Angulo-Martínez, M., Barros, A., 2015. Measurement uncertainty in rainfall kinetic energy and intensity relationships for soil erosion studies: An evaluation using PARSIVEL disdrometers in the Southern Appalachian Mountains. Geomorphology 228, 28–40. URL: https://linkinghub.elsevier.com/retrieve/pii/S0169555X14004140, doi:10.1016/j.geomorph.2014.07.036.

740 Angulo-Martínez, M., Beguería, S., Navas, A., Machín, J., 2012. Splash erosion un-
741 der natural rainfall on three soil types in NE Spain. Geomorphology 175-176, 38–
742 44. URL: http://www.sciencedirect.com/science/article/pii/S0169555X12003005,
743 doi:10.1016/j.geomorph.2012.06.016.

744 ASTM-G73-10, 2017. Standard test method for liquid impingement erosion using rotating appara-
745 tus. Astm , 1 – 19doi:https://doi.org/10.1520/G0073-10R17.

746 Atlas, D., Srivastava, R.C., Sekhon, R.S., 1973. Doppler radar characteristics of precipitation at
747 vertical incidence. Reviews of Geophysics 11, 1. URL: http://doi.wiley.com/10.1029/
748 RG011i001p00001, doi:10.1029/RG011i001p00001.

749 Atlas, D., Ulbrich, C.W., 1977. Path- and Area-Integrated Rainfall Measurement by Microwave
750 Attenuation in the 1–3 cm Band. Journal of Applied Meteorology 16, 1322–1331. URL: https:
751 //journals.ametsoc.org/doi/abs/10.1175/1520-0450%281977%29016%3C1322%
752 3APAAIRM%3E2.0.CO%3B2, doi:10.1175/1520-0450(1977)016<1322:PAAIRM>2.0.CO;2.

753 Battaglia, A., Rustemeier, E., Tokay, A., Blahak, U., Simmer, C., 2010. PARSIVEL Snow Observa-
754 tions: A Critical Assessment. Journal of Atmospheric and Oceanic Technology 27, 333–344.
755 URL: https://journals.ametsoc.org/doi/10.1175/2009JTECHA1332.1, doi:10.1175/
756 2009JTECHA1332.1.

757 Bech, J.I., Hasager, C.B., Bak, C., 2018. Extending the life of wind turbine blade leading edges by
758 reducing the tip speed during extreme precipitation events. Wind Energy Science 3, 729–748.
759 URL: https://www.wind-energ-sci.net/3/729/2018/, doi:10.5194/wes-3-729-2018.

760 Best, A.C., 1950. The size distribution of raindrops. Quarterly Journal of the Royal Meteorological
761 Society 76, 16–36. URL: https://rmets.onlinelibrary.wiley.com/doi/abs/10.1002/
762 qj.49707632704, doi:10.1002/qj.49707632704.

763 Brawn, D., Upton, G., 2008. Estimation of an atmospheric gamma drop size distribution using
764 disdrometer data. Atmospheric Research 87, 66–79. URL: https://linkinghub.elsevier.
765 com/retrieve/pii/S0169809507001238, doi:10.1016/j.atmosres.2007.07.006.

766 Brown, L., Foster, G., 1987. storm Erosivity Using Idealized Intensity Distributions. Transactions
767 of the ASAE 30, 0379–0386. URL: http://elibrary.asabe.org/abstract.asp??JID=3&
768 AID=31957&CID=t1987&v=30&i=2&T=1, doi:10.13031/2013.31957.

769 C. McGregor, K., L. Bingner, R., J. Bowie, A., R. Foster, G., 1995. Erosivity Index Values for
770 Northern Mississippi. Transactions of the ASAE 38, 1039–1047. URL: http://elibrary.
771 asabe.org/abstract.asp?aid=27921&t=3, doi:10.13031/2013.27921. place: St. Joseph,
772 MI Publisher: ASAE.

773 Campbell-Scientific-Ltd, 2012. Pws100 present weather sensor, user guide, 2012.

774 Cao, Q., Zhang, G., 2009. Errors in Estimating Raindrop Size Distribution Parameters Employing
775 Disdrometer and Simulated Raindrop Spectra. Journal of Applied Meteorology and Climatol-
776 ogy 48, 406–425. URL: http://journals.ametsoc.org/doi/10.1175/2008JAMC2026.1,
777 doi:10.1175/2008JAMC2026.1.

778 Cao, Q., Zhang, G., Brandes, E., Schuur, T., Ryzhkov, A., Ikeda, K., 2008. Analysis of video
779 disdrometer and polarimetric radar data to characterize rain microphysics in oklahoma. Journal of
780 Applied Meteorology and Climatology 47, 2238 – 2255. URL: https://journals.ametsoc.
781 org/view/journals/apme/47/8/2008jamc1732.1.xml, doi:10.1175/2008JAMC1732.1.

782 Carollo, F.G., Ferro, V., 2015. Modeling Rainfall Erosivity by Measured Drop-Size Distribu-
783 tions. Journal of Hydrologic Engineering 20. URL: http://ascelibrary.org/doi/10.1061/
784 %28ASCE%29HE.1943-5584.0001077, doi:10.1061/(ASCE)HE.1943-5584.0001077.

785 Carollo Francesco Giuseppe, Ferro Vito, 2015. Modeling Rainfall Erosivity by Measured
786 Drop-Size Distributions. Journal of Hydrologic Engineering 20, C4014006. URL:
787 https://ascelibrary.org/doi/full/10.1061/%28ASCE%29HE.1943-5584.0001077,
788 doi:10.1061/(ASCE)HE.1943-5584.0001077.

789 Carter, C.A., 1979. Activation of reovirion-associated poly(A) polymerase and oligomer
790 methylase by cofactor-dependent cleavage of polypeptides. Virology 94, 417–
791 429. URL: http://www.sciencedirect.com/science/article/pii/0042682279904720,
792 doi:10.1016/0042-6822(79)90472-0.

793 Deidda, R., Benzi, R., Siccardi, F., 1999. Multifractal modeling of anomalous scaling laws in
794 rainfall. Water Resources Research 35, 1853–1867. URL: https://agupubs.onlinelibrary.
795 wiley.com/doi/abs/10.1029/1999WR900036, doi:10.1029/1999WR900036.

796 Deog Park, S., Song Lee, K., Sook Shin, S., 2012. Statistical Soil Erosion Model for Burnt
797 Mountain Areas in Korea—RUSLE Approach. Journal of Hydrologic Engineering 17, 292–
798 304. URL: http://ascelibrary.org/doi/10.1061/%28ASCE%29HE.1943-5584.0000441,
799 doi:10.1061/(ASCE)HE.1943-5584.0000441.

800 van Dijk, A., Bruijnzeel, L., Rosewell, C., 2002. Rainfall intensity–kinetic energy re-
801 lationships: a critical literature appraisal. Journal of Hydrology 261, 1–23. URL:
802 https://linkinghub.elsevier.com/retrieve/pii/S0022169402000203, doi:10.1016/
803 S0022-1694(02)00020-3.

804 DNVGL-RP-0171, 2014. Recommended practice, testing of rotor blade erosion protection systems,
805 edition 2018-02 URL: http://www.dnvgl.com.

806 Ellis, R.A., Sandford, A.P., Jones, G.E., Richards, J., Petzing, J., Coupland, J., 2006. New laser
807 technology to determine present weather parameters URL: https://repository.lboro.ac.

uk/articles/New_laser_technology_to_determine_present_weather_parameters/9574658.

Ellison, W.D., 1944. Ellison: Studies of raindrop erosion - Google Scholar. URL: https://scholar.google.com/scholar_lookup?title=Studies%20of%20raindrop%20erosion&publication_year=1944&author=W.D.%20Ellison.

Emmanouil, S., Langousis, A., Nikolopoulos, E.I., Anagnostou, E.N., 2020. Quantitative assessment of annual maxima, peaks-over-threshold and multifractal parametric approaches in estimating intensity-duration-frequency curves from short rainfall records. Journal of Hydrology 589, 125151. URL: https://www.sciencedirect.com/science/article/pii/S0022169420306119, doi:https://doi.org/10.1016/j.jhydrol.2020.125151.

Enne, G., Zanolla, C., Peter, D., 2000. Desertification in europe: Mitigation strategies, land-use planning .

Feingold, G., Levin, Z., 1986. The Lognormal Fit to Raindrop Spectra from Frontal Convective Clouds in Israel. Journal of Applied Meteorology 25, 1346–1364. URL: http://adsabs.harvard.edu/abs/1986JApMe..25.1346F, doi:10.1175/1520-0450(1986)025<1346:TLFTRS>2.0.CO;2.

Fernández-Raga, M., Palencia, C., Keesstra, S., Jordán, A., Fraile, R., Angulo-Martínez, M., Cerdà, A., 2017. Splash erosion: A review with unanswered questions. Earth-Science Reviews 171, 463–477. URL: http://www.sciencedirect.com/science/article/pii/S0012825217301150, doi:10.1016/j.earscirev.2017.06.009.

Fox, N.I., 2004. TECHNICAL NOTE: The representation of rainfall drop-size distribution and kinetic energy. Hydrology and Earth System Sciences 8, 1001–1007. URL: http://www.hydrol-earth-syst-sci.net/8/1001/2004/, doi:10.5194/hess-8-1001-2004.

García-Marín, A.P., Jiménez-Hornero, F.J., Ayuso-Muñoz, J.L., 2008. Universal multifractal description of an hourly rainfall time series from a location in southern Spain. Atmósfera 21, 347–355. URL: http://www.scielo.org.mx/scielo.php?script=sci_abstract&pid=S0187-62362008000400003&lng=es&nrm=iso&tlng=en.

Gatidis, C., Schleiss, M., Unal, C., Russchenberg, H., 2020. A critical evaluation of the adequacy of the gamma model for representing raindrop size distributions. Journal of Atmospheric and Oceanic Technology 37, 1765 – 1779. URL: https://journals.ametsoc.org/view/journals/atot/37/10/jtechD190106.xml, doi:10.1175/JTECH-D-19-0106.1.

Gires, A., Tchiguirinskaia, I., Schertzer, D., 2017. Method and device for measuring the equivalent diameter of a water drop. European Patent Office (Application nb. EP3246692) .

Gires, A., Tchiguirinskaia, I., Schertzer, D., 2018. Two months of disdrometer data in the paris area. Earth System Science Data 10, 941–950. URL: https://www.earth-syst-sci-data.net/10/941/2018/, doi:10.5194/essd-10-941-2018.

Gunn, R., Kinzer, G.D., 1949. THE TERMINAL VELOCITY OF FALL FOR WATER DROPLETS IN STAGNANT AIR. Journal of Meteorology 6, 243–248. URL: https://doi.org/10.1175/1520-0469(1949)006<0243:TTVOFF>2.0.CO;2, doi:10.1175/1520-0469(1949)006<0243:TTVOFF>2.0.CO;2.

Gupta, V.K., Waymire, E., 1990. Multiscaling properties of spatial rainfall and river flow distributions. Journal of Geophysical Research: Atmospheres 95, 1999–2009. URL: https://agupubs.onlinelibrary.wiley.com/doi/abs/10.1029/JD095iD03p01999, doi:10.1029/JD095iD03p01999.

Herring, R., Dyer, K., Martin, F., Ward, C., 2019. The increasing importance of leading edge erosion and a review of existing protection solutions. Renewable and Sustainable Energy

Reviews 115, 109382. URL: http://www.sciencedirect.com/science/article/pii/S1364032119305908, doi:10.1016/j.rser.2019.109382.

Huang, C., Chen, S., Zhang, A., Pang, Y., 2021. Statistical characteristics of raindrop size distribution in monsoon season over south china sea. Remote Sensing 13. URL: https://www.mdpi.com/2072-4292/13/15/2878, doi:10.3390/rs13152878.

Hudson, N.W., 1971. Soil conservation. Batsford, London.

Ignaccolo, M., De Michele, C., 2014. Phase space parameterization of rain: The inadequacy of gamma distribution. Journal of Applied Meteorology and Climatology 53, 548–562.

Jaffrain, J., Berne, A., 2012. Quantification of the Small-Scale Spatial Structure of the Raindrop Size Distribution from a Network of Disdrometers. Journal of Applied Meteorology and Climatology 51, 941–953. URL: https://journals.ametsoc.org/doi/10.1175/JAMC-D-11-0136.1, doi:10.1175/JAMC-D-11-0136.1.

Johannsen, L.L., Zambon, N., Strauss, P., Dostal, T., Neumann, M., Zumr, D., Cochrane, T.A., BlÃ¶schl, G., Klik, A., 2020a. Comparison of three types of laser optical disdrometers under natural rainfall conditions. Hydrological Sciences Journal 65, 524–535. URL: https://doi.org/10.1080/02626667.2019.1709641, doi:10.1080/02626667.2019.1709641, arXiv:https://doi.org/10.1080/02626667.2019.1709641. pMID: 32257534.

Johannsen, L.L., Zambon, N., Strauss, P., Dostal, T., Neumann, M., Zumr, D., Cochrane, T.A., BlÃ¶schl, G., Klik, A., 2020b. Comparison of three types of laser optical disdrometers under natural rainfall conditions. Hydrological Sciences Journal 65, 524–535. URL: https://doi.org/10.1080/02626667.2019.1709641, doi:10.1080/02626667.2019.1709641, arXiv:https://doi.org/10.1080/02626667.2019.1709641.

Karlen, D., Andrews, S., Weinhold, B., Doran, J., 2003. Soil quality: Humankind's foundation for survival. Journal of Soil and Water Conservation 58, 171–179.

Keegan, M.H., Nash, D.H., Stack, M.M., 2013. On erosion issues associated with the leading edge of wind turbine blades. Journal of Physics D: Applied Physics 46, 383001. URL: http://stacks.iop.org/0022-3727/46/i=38/a=383001?key=crossref.b21f1d8515962c024d50ce37171c3281, doi:10.1088/0022-3727/46/38/383001.

Kinnell, P., 1981. Rainfall Intensity-Kinetic Energy Relationships for Soil Loss Prediction1. Soil Science Society of America Journal 45, 153. URL: https://www.soils.org/publications/sssaj/abstracts/45/1/SS0450010153, doi:10.2136/sssaj1981.03615995004500010033x.

Kirkby, M.J., Irvine, B.J., Jones, R.J.A., Govers, G., team, P., 2008. The pesera coarse scale erosion model for europe. i. â model rationale and implementation. European Journal of Soil Science 59, 1293–1306. URL: https://onlinelibrary.wiley.com/doi/abs/10.1111/j.1365-2389.2008.01072.x, doi:https://doi.org/10.1111/j.1365-2389.2008.01072.x, arXiv:https://onlinelibrary.wiley.com/doi/pdf/10.1111/j.1365-2389.2008.01072.x.

Konwar, M., Das, S.K., Deshpande, S.M., Chakravarty, K., Goswami, B.N., 2014. Microphysics of clouds and rain over the western ghat. Journal of Geophysical Research: Atmospheres 119, 6140–6159. URL: https://agupubs.onlinelibrary.wiley.com/doi/abs/10.1002/2014JD021606, doi:https://doi.org/10.1002/2014JD021606, arXiv:https://agupubs.onlinelibrary.wiley.com/doi/pdf/10.1002/2014JD021606.

Kruger, A., Krajewski, W.F., 2002. Two-Dimensional Video Disdrometer: A Description. Journal of Atmospheric and Oceanic Technology 19, 602–617. URL: https://journals.ametsoc.org/doi/full/10.1175/1520-0426%282002%29019%3C0602%3ATDVDAD%3E2.0.CO%3B2, doi:10.1175/1520-0426(2002)019<0602:TDVDAD>2.0.CO;2.

Kumar, P., Foufoula-Georgiou, E., 1993. A multicomponent decomposition of spatial rainfall fields: 2. Self-similarity in fluctuations. Water Resources Research 29, 2533–2544. URL: https://agupubs.onlinelibrary.wiley.com/doi/abs/10.1029/93WR00549, doi:10.1029/93WR00549.

Langousis, A., Veneziano, D., Furcolo, P., Lepore, C., 2009. Multifractal rainfall extremes: Theoretical analysis and practical estimation. Chaos, Solitons Fractals 39, 1182–1194. URL: https://www.sciencedirect.com/science/article/pii/S0960077907003700, doi:https://doi.org/10.1016/j.chaos.2007.06.004.

Lavallée, D., Lovejoy, S., Schertzer, D., Ladoy, P., 1993. Nonlinear variability and landscape topography: analysis and simulation. Fractals in geography , 158–192.

Laws, J.O., Parsons, D.A., 1943. The relation of raindrop-size to intensity. Eos, Transactions American Geophysical Union 24, 452–460. URL: https://agupubs.onlinelibrary.wiley.com/doi/abs/10.1029/TR024i002p00452, doi:10.1029/TR024i002p00452.

Liersch, J., Michael, J., 2014. Investigation of the impact of rain and particle erosion on rotor blade aerodynamics with an erosion test facility to enhancing the rotor blade performance and durability. Journal of Physics: Conference Series 524, 012023. URL: http://stacks.iop.org/1742-6596/524/i=1/a=012023?key=crossref.010c71a204a1e683cb616b2c527d4c05, doi:10.1088/1742-6596/524/1/012023.

Lovejoy, S., Schertzer, D., Allaire, V.C., 2008. The remarkable wide range spatial scaling of TRMM precipitation. Atmospheric Research 90, 10–32. URL: https://hal-enpc.archives-ouvertes.fr/hal-00711539, doi:10.1016/j.atmosres.2008.02.016.

Marshall, J.S., Palmer, W.M.K., 1948. The distribution of raindrops with size. Journal of Meteorology 5, 165–166. URL: https://journals.ametsoc.org/

924 doi/abs/10.1175/1520-0469%281948%29005%3C0165%3ATDORWS%3E2.0.CO%3B2,
925 doi:10.1175/1520-0469(1948)005<0165:TDORWS>2.0.CO;2.

926 Mineo, C., Ridolfi, E., Moccia, B., Russo, F., Napolitano, F., 2019. Assessment of Rainfall Kinetic-
927 Energy–Intensity Relationships. Water 11, 1994. URL: https://www.mdpi.com/2073-4441/
928 11/10/1994, doi:10.3390/w11101994.

929 Mohamadi, M.A., Kavian, A., 2015. Effects of rainfall patterns on runoff and soil ero-
930 sion in field plots. International Soil and Water Conservation Research 3, 273–281.
931 URL: https://www.sciencedirect.com/science/article/pii/S209563391530071X,
932 doi:https://doi.org/10.1016/j.iswcr.2015.10.001.

933 Morgan, R.P.C., Quinton, J.N., Smith, R.E., Govers, G., Poesen, J.W.A., Auer-
934 swald, K., Chisci, G., Torri, D., Styczen, M.E., 1998. The European Soil Ero-
935 sion Model (EUROSEM): a dynamic approach for predicting sediment transport
936 from fields and small catchments. Earth Surface Processes and Landforms 23, 527–
937 544. URL: https://onlinelibrary.wiley.com/doi/abs/10.1002/%28SICI%
938 291096-9837%28199806%2923%3A6%3C527%3A%3AAID-ESP868%3E3.0.CO%3B2-5,
939 doi:10.1002/(SICI)1096-9837(199806)23:6<527::AID-ESP868>3.0.CO;2-5.

940 Olsson, J., Niemczynowicz, J., 1996. Multifractal analysis of daily spatial rainfall distribu-
941 tions. Journal of Hydrology 187, 29–43. URL: http://www.sciencedirect.com/science/
942 article/pii/S0022169496030855, doi:10.1016/S0022-1694(96)03085-5.

943 OTT, 2014. Operating instructions, Present Weather Sensor OTT Parsivel2 .

944 Parisi, G., Frisch, U., 1985. On the singularity structure of fully developed turbulence in Turbu-
945 lence and predictability in geophysical fluid dynamics and climate dynamics. NTurbulence and
946 Predictability of Geophysical Flows and Climate Dynamics 88.

Park, S., Mitchell, J., Bubenzer, G., 1982. Splash erosion modelling: physical analyses [Impact of water drops on soil]. Transactions of the ASAE [American Society of Agricultural Engineers] URL: http://agris.fao.org/agris-search/search.do?recordID=US19830881711.

Petan, S., Rusjan, S., Vidmar, A., Mikoš, M., 2010. The rainfall kinetic energy–intensity relationship for rainfall erosivity estimation in the mediterranean part of Slovenia. Journal of Hydrology 391, 314 – 321. URL: http://www.sciencedirect.com/science/article/pii/S0022169410004695, doi:https://doi.org/10.1016/j.jhydrol.2010.07.031.

Pimentel, D., 2006. Soil Erosion: A Food and Environmental Threat. Environment, Development and Sustainability 8, 119–137. URL: https://doi.org/10.1007/s10668-005-1262-8, doi:10.1007/s10668-005-1262-8.

Renard, K.G., Agricultural Research Service, W., Foster, G.R., Weesies, G.A., McCool, D.K., Yoder, D.C., 1997. Predicting soil erosion by water: a guide to conservation planning with the Revised Universal Soil Loss Equation (RUSLE) URL: http://agris.fao.org/agris-search/search.do?recordID=XF2015047686.

Salles, C., Poesen, J., Sempere-Torres, D., 2002. Kinetic energy of rain and its functional relationship with intensity. Journal of Hydrology 257, 256–270. URL: https://linkinghub.elsevier.com/retrieve/pii/S0022169401005558, doi:10.1016/S0022-1694(01)00555-8.

Schertzer, D., Lovejoy, S., 1987. Physical modeling and analysis of rain and clouds by anisotropic scaling multiplicative processes. Journal of Geophysical Research: Atmospheres 92, 9693–9714. URL: https://agupubs.onlinelibrary.wiley.com/doi/abs/10.1029/JD092iD08p09693, doi:10.1029/JD092iD08p09693.

Schertzer, D., Lovejoy, S., 1988. Multifractal simulations and analysis of clouds by multiplica-

970 tive processes. Atmospheric Research 21, 337–361. URL: http://www.sciencedirect.com/
971 science/article/pii/016980958890035X, doi:10.1016/0169-8095(88)90035-X.

972 Schertzer, D., Lovejoy, S., 2011. MULTIFRACTALS, GENERALIZED SCALE INVARI-
973 ANCE AND COMPLEXITY IN GEOPHYSICS. International Journal of Bifurcation and
974 Chaos 21, 3417–3456. URL: https://www.worldscientific.com/doi/abs/10.1142/
975 S0218127411030647, doi:10.1142/S0218127411030647.

976 Schertzer, D., Tchiguirinskaia, I., 2020. A century of turbulent cas-
977 cades and the emergence of multifractal operators. Earth and Space Sci-
978 ence 7, e2019EA000608. URL: https://agupubs.onlinelibrary.
979 wiley.com/doi/abs/10.1029/2019EA000608, doi:10.1029/2019EA000608,
980 arXiv:https://agupubs.onlinelibrary.wiley.com/doi/pdf/10.1029/2019EA000608.
981 e2019EA000608 10.1029/2019EA000608.

982 Sempere-Torres, D., Porrà, J.M., Creutin, J.D., 1998. Experimental evidence of a general descrip-
983 tion for raindrop size distribution properties. Journal of Geophysical Research: Atmospheres 103,
984 1785–1797. URL: http://doi.wiley.com/10.1029/97JD02065, doi:10.1029/97JD02065.

985 Shin, S.S., Park, S.D., Choi, B.K., 2016. Universal Power Law for Relationship between Rainfall
986 Kinetic Energy and Rainfall Intensity. URL: https://www.hindawi.com/journals/amete/
987 2016/2494681/, doi:https://doi.org/10.1155/2016/2494681.

988 Shojaei, S., Kalantari, Z., Rodrigo-Comino, J., 2020. Prediction of factors affecting activation of
989 soil erosion by mathematical modeling at pedon scale under laboratory conditions. Scientific
990 Reports 10, 20163. URL: https://doi.org/10.1038/s41598-020-76926-1, doi:10.1038/
991 s41598-020-76926-1.

992 Smith, D.D., Wischmeier, W.H., 1962. Rainfall Erosion, in: Norman, A.G. (Ed.), Advances in

993 Agronomy. Academic Press. volume 14, pp. 109–148. URL: http://www.sciencedirect.
994 com/science/article/pii/S006521130860437X, doi:10.1016/S0065-2113(08)60437-X.

995 Smith, J.A., De Veaux, R.D., 1992. The temporal and spatial variability of
996 rainfall power. Environmetrics 3, 29–53. URL: https://onlinelibrary.
997 wiley.com/doi/abs/10.1002/env.3170030103, doi:10.1002/env.3170030103,
998 arXiv:https://onlinelibrary.wiley.com/doi/pdf/10.1002/env.3170030103.

999 Smith, P.L., Kliche, D.V., Johnson, R.W., 2009. The Bias and Error in Moment Estimators for
1000 Parameters of Drop Size Distribution Functions: Sampling from Gamma Distributions. Journal
1001 of Applied Meteorology and Climatology 48, 2118–2126. URL: http://journals.ametsoc.
1002 org/doi/10.1175/2009JAMC2114.1, doi:10.1175/2009JAMC2114.1.

1003 Steiner, M., Smith, J.A., 2000. Reflectivity, Rain Rate, and Kinetic Energy Flux Relationships
1004 Based on Raindrop Spectra. JOURNAL OF APPLIED METEOROLOGY 39, 18.

1005 Tessier, Y., Lovejoy, S., Schertzer, D., 1993. Universal multifractals: Theory and observations for
1006 rain and clouds. Journal of Applied Meteorology and Climatology 32, 223 – 250. URL: https:
1007 //journals.ametsoc.org/view/journals/apme/32/2/1520-0450_1993_032_0223_
1008 umtaof_2_0_co_2.xml, doi:10.1175/1520-0450(1993)032<0223:UMTAOF>2.0.CO;2.

1009 Testud, J., 2001. The Concept of "Normalized" Distribution to Describe Raindrop Spectra: A Tool
1010 for Cloud Physics and Cloud Remote Sensing. JOURNAL OF APPLIED METEOROLOGY 40,
1011 23.

1012 Thurai, M., Bringi, V.N., 2005. Drop Axis Ratios from a 2D Video Disdrometer. Journal of Atmo-
1013 spheric and Oceanic Technology 22, 966–978. URL: https://journals.ametsoc.org/doi/
1014 full/10.1175/JTECH1767.1, doi:10.1175/JTECH1767.1.

1015 Tokay, A., Short, D.A., 1996. Evidence from Tropical Raindrop Spectra of the Origin of
1016 Rain from Stratiform versus Convective Clouds. Journal of Applied Meteorology 35, 355–
1017 371. URL: https://journals.ametsoc.org/doi/abs/10.1175/1520-0450%281996%
1018 29035%3C0355%3AEFTRSO%3E2.0.CO%3B2, doi:10.1175/1520-0450(1996)035<0355:
1019 EFTRSO>2.0.CO;2.

1020 Torres, D.S., Porrà, J.M., Creutin, J.D., 1994. A General Formulation for Raindrop Size Distribu-
1021 tion. Journal of Applied Meteorology 33, 1494–1502. URL: https://journals.ametsoc.
1022 org/doi/abs/10.1175/1520-0450%281994%29033%3C1494%3AAGFFRS%3E2.0.CO%3B2,
1023 doi:10.1175/1520-0450(1994)033<1494:AGFFRS>2.0.CO;2.

1024 Uijlenhoet, R., 2001. Raindrop size distributions and radar reflectivity–rain rate rela-
1025 tionships for radar hydrology. Hydrology and Earth System Sciences 5, 615–628.
1026 URL: https://www.hydrol-earth-syst-sci.net/5/615/2001/, doi:https://doi.org/
1027 10.5194/hess-5-615-2001.

1028 Uijlenhoet, R., Stricker, J., 1999. A consistent rainfall parameterization based on the
1029 exponential raindrop size distribution. Journal of Hydrology 218, 101–127. URL:
1030 https://linkinghub.elsevier.com/retrieve/pii/S0022169499000323, doi:10.1016/
1031 S0022-1694(99)00032-3.

1032 Ulbrich, C.W., 1983. Natural Variations in the Analytical Form of the Raindrop Size Dis-
1033 tribution. Journal of Climate and Applied Meteorology 22, 1764–1775. URL: https:
1034 //journals.ametsoc.org/doi/abs/10.1175/1520-0450%281983%29022%3C1764%
1035 3ANVITAF%3E2.0.CO%3B2, doi:10.1175/1520-0450(1983)022<1764:NVITAF>2.0.CO;2.

1036 Van Oost, K., Govers, G., Desmet, P., 2000. Evaluating the effects of changes in landscape structure
1037 on soil erosion by water and tillage. Landscape Ecology 15, 577–589. URL: https://doi.
1038 org/10.1023/A:1008198215674, doi:10.1023/A:1008198215674.

1039 Wilken, F., Baur, M., Sommer, M., Deumlich, D., Bens, O., Fiener, P., 2018. Uncertainties in
1040 rainfall kinetic energy-intensity relations for soil erosion modelling. CATENA 171, 234–244.
1041 URL: https://linkinghub.elsevier.com/retrieve/pii/S034181621830273X, doi:10.
1042 1016/j.catena.2018.07.002.

1043 Wolfensberger, D., Gires, A., Tchiguirinskaia, I., Schertzer, D., Berne, A., 2017. Multifractal eval-
1044 uation of simulated precipitation intensities from the COSMO NWP model. Atmospheric Chem-
1045 istry and Physics 17, 14253–14273. URL: https://www.atmos-chem-phys.net/17/14253/
1046 2017/, doi:10.5194/acp-17-14253-2017.